STRENGTH OF STRUCTURAL COMPOSITE ANGLE BRACKET WITH NANO-ENHANCED RESIN

Thesis

Submitted to

The School of Engineering of the

UNIVERSITY OF DAYTON

In Partial Fulfillment of the Requirements for

The Degree

Master of Science in Civil Engineering

By

Stephanie Christine Avalon

UNIVERSITY OF DAYTON

Dayton, Ohio

August, 2008

APPROVED BY:

Brockman, Robert A.
Committee Member

Donaldson, Steven L.
Committee Member & Faculty Advisor

Kim, Ran Y
Committee Member

ABSTRACT

STRENGTH OF STRUCTURAL COMPOSITE ANGLE BRACKET WITH NANO-ENHANCED RESIN

Name: Avalon, Stephanie Christine
University of Dayton

Advisor: Dr. S.L. Donaldson

The purpose of this study was to investigate the change of the strength and failure mode of a composite angle bracket with the addition of vapor grown carbon nanofiber to the epoxy resin matrix. The bracket explored within this study was a woven composite with a 90° bend subjected to four-point bend loading. Such angle brackets exhibit weakness around the radius due to the excessive through-the-thickness tensile stresses which can lead to delamination.

Composite brackets of 8 and 16 plies were examined, for bend radii of 0.125 inches and 0.25 inches. The composite consisted of Hexcel AS4 carbon fiber five-harness satin weave and Epon 862/Epikure W epoxy resin. Specimens were fabricated with and without ASI PR-24 vapor grown carbon nanofiber in the epoxy matrix. A servo-hydraulic load frame was used to perform a four-point-bend test per American Society for Testing and Materials (ASTM) D6415 for Measuring the Curved Beam Strength of a Fiber-Reinforced Polymer Matrix Composite.

Despite a three-fold difference in failure load and curved beam strength, data reduction using both closed-form and finite element modeling resulted in a nearly single critical value of radial peel stress at initial failure of 4,300-4,700 psi. The fracture type (large load drop versus "stick-slip") and optical microscopy results are explored in detail.

ACKNOWLEDGEMENTS

I would like to express my thanks and appreciation to Dr. Steve Donaldson, my advisor, for providing the time and equipment necessary for the work contained herein, and for directing this thesis and bringing it to its conclusion with patience and expertise.

I would also like to thank everyone who has helped me over the past year with my thesis and graduate degree. This includes Dr. Faris Malhas, Dr. Malcolm Daniels, and Brian Rice, for making this experience possible; Jill Morgan, who helped to guide me and give me direction over the past couple of years; Johanna Snead, who assisted me, especially throughout the past couple months of my graduate degree; Dr. Robert Brockman, for providing his time and knowledge of finite element analysis; Ken Goecke, for taking time out of his schedule to help me run all of the tests required for this paper, and for providing me with his own insight and guidance; Ran Kim, for also helping me with the testing procedure and for providing me with his knowledge; Bill Price, for taking time out of his schedule to teach me, and allowing me to use University of Dayton Research Institute's equipment; Tim Campbell, for his kindness and knowledge, and for helping me to polish the specimen; Jared Stonecash for helping me from the very beginning of my thesis, for his time and expertise, and for allowing me to use the

necessary equipment; Nick Gagliardi, for fitting me into UDRI's schedule to use their equipment, and for his time and knowledge on composites; Casey Brown, for all of her help in the fabrication of the composite structures; John Stalter, for machining every one of the specimen tested for this thesis; Roger Rondeau, for his time and knowledge; everyone else at UDRI who was not mentioned, who allowed for me to use their facilities and equipment.

Finally, I would like to thank my family and boyfriend for their support and encouragement throughout my graduate program.

TABLE OF CONTENTS

LIST OF FIGURES

LIST OF TABLES

LIST OF SYMBOLS

CBS = curved beam strength

d_x, d_y = horizontal and vertical distances between two adjacent top and bottom loading bars, respectively

D = diameter of the cylindrical loading bars on the four-point-bending fixture

E_r, E_θ = moduli in the radial and tangential directions, respectively

g = parameter used in strength calculation

M = applied moment

P = total force applied to the four-point-bending fixture

P^{max} = maximum force applied to the four-point-bending fixture before failure

r, θ = cylindrical coordinates of any point in the curved segment

r_i, r_o (R_i, R_o) = inner and outer radii of curved segment

r_m = radial position of the maximum interlaminar (radial) tensile stress

R_m = mean radius (used in approximate equations)

t = average thickness of specimen

w = width of the specimen

Δ = relative displacement between the top and bottom halves of the four-point-bending fixture

k = parameter used in the strength calculation

ρ = parameter used in strength calculation

Φ = angle from horizontal of the specimen legs in degrees

Φ_i = angle from horizontal of the specimen legs at the start of the test in degrees (0.5 X angle between the legs)

σ_r = radial stress component in curved segment

CHAPTER I

INTRODUCTION

Composites differ from other homogeneous materials in that they are comprised of more than one constituent material. The structural performance of the composite surpasses that of the constituent materials acting alone. There are two phases that exist within a composite. One of the phases is usually stiffer and stronger and is called the reinforcement, whereas the other phase, the matrix, is weaker and continuous [1]. For the composite considered within this text, the reinforcement is carbon satin weave, and the matrix is epoxy resin. The geometry and distribution of the constituent materials both influence the properties of the composite material. One of the most important considerations of a composite is the weight fraction of the reinforcement or the fiber volume ratio. The distribution of the reinforcement determines the homogeneity or uniformity of the material system. When the distribution of reinforcement is nonuniform, there is a higher chance that there will be a scatter in the properties and failure will occur in the weak areas. For example, if a resin pocket is created due to the shifting of fiber during fabrication, then the composite will encompass a weak spot in that area.

The phases of the composite system have different roles, depending on the level of performance expected. Composites that are low- to medium-performance typically have reinforcement in the form of short fibers or particles. The reinforcement provides some stiffening but only limited strengthening of the material [1]. High-performance composites normally have continuous fiber reinforcement, which determines the stiffness and strength in the fiber direction. The composite used in this paper is considered a high-performance composite.

Composites have unique advantages over monolithic materials, such as high strength, high stiffness, long fatigue life, low density, and adaptability to the intended function of the structure [1]. Additional improvements can be realized in corrosion resistance, wear resistance, appearance, temperature-dependent behavior, environmental stability, thermal insulation and conductivity, and acoustic insulation. The main reason for such high structural performance is due to the high specific strength (strength-to-weight ratio) and specific stiffness (modulus-to-weight ratio) of the composites.

The requirements for high performance materials for aircraft and aerospace structures have been one of the driving forces for the research and development behind composite materials. Structures comprised of composites are attractive to the aerospace industry for their high stiffness, high strength, low density, and corrosion resistance, among other attributes. In addition, the use of advanced composites has expanded into high volume markets such as energy, transportation, and civil structures. The need for evaluation and improvement of composite materials is imperative considering the expanding market. Proposed

applications for composites include complex structural details including laminates with sharp radii. In addition, the use of nano-scale reinforcements to matrix resins has gained extensive research interest.

Angle brackets, such as the one analyzed within this paper, exhibit weakness around the radius due to excessive through-the-thickness tensile stresses which can lead to delamination. Delamination, which is the separation of layers or plies under shear and normal stresses, is one of the most common failures in composites [1]. While most high-performance composites are designed to have superior in-plane stiffness and strength, they are not as strong when they are subjected to interlaminar shear and normal stresses.

The purpose of this study is to investigate the change of the strength and failure mode of the composite angle bracket (with a sharp 90° bend) with the addition of vapor grown carbon nanofiber to the epoxy resin matrix. The composite was fabricated from carbon fiber, five harness weave and epoxy resin. Brackets were made for different thicknesses (varying the number of plies) and radii, both with and without nano-modified resin (NMR). The bracket was subjected to four-point bend loading in order to evaluate the through-the-thickness tensile stresses around the radius. The test procedure used was the American Society for Testing and Materials (ASTM) D6415 for Measuring the Curved Beam Strength of a Fiber-Reinforced Polymer Matrix Composite [2]. The maximum radial stress and location were calculated using ASTM D6415. The results were compared to finite element analysis models that were created using ABAQUS.

CHAPTER II

REVIEW OF RELATED RESEARCH AND LITERATURE

The composite configuration discussed within this paper is a structural bracket whose properties are of interest within the aerospace and other industries. Brackets similar to this one have been previously analyzed, showing that when tested in tension or flexure, the primary failure mode occurs around the radius [3] – [17]. Excessive through-the-thickness stresses in the vicinity of the radius cause the plies to delaminate. Because of delamination, it was of interest to determine a method to lessen the high localized stresses and/or improve the out-of-plane strength. The method tested within this paper is the use of nano-modified resin (NMR). The proper addition of nanofibers within a composite may lead to increased strength.

The brackets previously analyzed generally fall into two different categories, those tested in a four-point flexure test, similar to the ASTM D6415 standard used in this paper [2], and those tested in a tension test. References [3] through [8] utilize the flexure method while references [9] through [14] use the tension test. Reference [15] investigates a wooden bend and [16] looks at various types of curved shapes. It is the last reference, [17], that is most like this

paper, in that it too, uses a technique to strengthen the curved region of the bracket.

In reference [3], Kedward, Wilson, and McLean state that numerous instances of premature failure of laminated composite components have occurred due to a general lack of appreciation for the low transverse tensile strength. They examine a curved beam using finite element methods, classical elasticity theory, and a simplified strength of materials approach, in order to demonstrate failure around the radius. Kedward, Wilson, and McLean state that the approximate methods presented in the paper can be used in order to ensure that matrix-dominated through-thickness transverse strength does not become a design driver.

References [4], [5], and [6] also measure the curved beam strength, but focus on a sandwich beam. The results in reference [4] avow good agreement between experimental and analytical results. The validity of the test fixture to produce the desired loading was examined by fitting a curved aluminum bar of similar bending stiffness as the sandwich beams considered [4]. Layne and Carlsson state that the strain gage readings successfully compared to predictions from curved homogeneous beam theory. In addition, the deflection of the beam at the loading points was analyzed using straight and curved beam theory for the various sections of the beam, and predictions were compared to measured load-displacement response [4]. Layne and Carlsson make use of an approximate equation for radial tension stress of a curved sandwich beam used from reference [6]. Both references [5] and [6] compare finite element analysis to an

approximation equation (referenced in [4]) and solutions to Airy's stress function. The literature states that the curvature of the bracket can have a significant influence on the radial stresses in the core. All three papers agree that the approximate equation can be used for beams with large to moderate radii of curvature.

The delamination stresses of semicircular laminated composite curved bars were studied in references [7] and [8]. The stresses and their radial locations were determined using Lekhnitskii equations [18], and a family of design curves was created in reference [7]. The resulting curves show that the location of the maximum radial stress moves away from the middle surface and toward the inner boundary of the curved bar as the ratio of the outer radius to inner radius increases. Reference [8] uses the classical anisotropic elasticity theory to construct a "multilayer" theory for the calculations of stress and deformation fields. Results were compared to the anisotropic continuum theory and finite element methods. Reference [8] maintains that the multilayer theory gives more accurate predictions of the location and intensity of the delamination stresses than those calculated from the anisotropic continuum theory.

Reference [9] and reference [14] tested composite curved beam specimens of 16, 24, and 32 plies and 16, 24, and 48 plies, respectively. Modified Lekhnitskii [18] and beam theory equations were used for calculating interlaminar stresses and were verified by finite element analysis in both papers. Reference [9] states that the results for the 16 and 24 ply specimens agreed reasonably well with data in the literature for a longer size specimen, while the

interlaminar tension strength decreased for the 32 ply specimen. Reference [9] claims that the decrease in strength with the thickness is due to the higher probability to have defects in a larger volume of material. Reference [14] also states that defects within the brackets had a large contribution in the value of strength. Jackson and Martin state that the best indicator of strength for a laminate is the local ply thickness; the highest strength configurations had the lowest ply thicknesses in the inner half of the thickness of the laminate.

In Reference [10], the through-the-thickness stresses were evaluated for two different types of specimens: elliptical and semicircular bends. The specimens were tested to failure using static and fatigue loads. Results showed that the tension failure load for the semicircular specimen was highly sensitive to flaw content, while the failure load for the elliptical specimen was unusually high, justifying grounds for further study. Fatigue data indicated no measured increase in specimen compliance prior to final fracture [10]. Results were also given for specimens that were put in a 100 percent relative humidity environment at 140°F for a period of 3 months [10]. Hiel, Sumich, and Chappell state that absorbed moisture has the effect of broadening the strength distribution. The load displacement plots obtained on the wet laminate revealed initial cracking beginning at about 60 percent of the ultimate failure load, followed by increases in load until final, complete fracture occurred [10]. This behavior was not observed for the dry specimens [10].

Reference [11] investigated the delamination failure in curved composite laminates. The delamination was assumed to occur at the location of the highest

radial stress in the curved region. The location was calculated using a Lekhnitskii closed form curved beam elasticity solution and finite element analysis [18]. Martin's prediction that the delamination growth will extend into the arm and leg of the laminate was verified through experimental observation. Failure of composite angle structures was also explored in reference [12] and reference [13]. In reference [12], the failure of 20 and 24 ply composite angles were both studied experimentally. Failure was also analyzed using Hill and an augmented Hill –Tsai failure criteria [12]. It was found that there are two different possible modes of progressive damage: initial transverse matrix cracking due to bending stress, and final delamination due to through-the-thickness normal stress in the curved region. In reference [13], analytical and experimental work was performed in order to predict delamination onset and growth of the composite bracket. Analytically, a closed-form stress analysis and a 2D and 3D finite element analysis were used in order to determine the stress distribution. Results state that the prediction for interlaminar tension delamination in 0° plies agreed reasonably well with the experimental results for the bracket.

A wooden structure with a 90° bend was considered in reference [15]. The structure was tested using a tension test similar to the test used in the literature previously mentioned. Experimental data and finite element analysis were used and compared to determine stresses within the structure. For each specimen tested, the analysis predicted failure to occur due to delamination. The visual examinations of the specimens tested also showed that every specimen failed by delamination.

Reference [16] investigated the interlaminar stresses of curved frame structures often seen in the internal structure in aircraft. Mason, Haftka, Johnson, and Farley used a finite element analysis combining two- and three-dimensional models to reduce the expense associated with the design of the frames. Frames with various design parameters and the tension test were considered. A response surface approach was then used to approximate the structural response of the frames as functions of the design variables [16].

It is stated in reference [17] that premature matrix failure due to bending can be controlled by varying the stacking sequence. However, the more critical delamination failure mode has been found to occur regardless of stacking sequence [17]. Sun and Kelly state that rather than controlling the stresses responsible for delamination it is necessary to augment the interlaminar strength of the laminate. Their method of choice was to use adhesive films to toughen the delamination-prone interfaces in the curved region. Experimental results indicated that the adhesive films could improve the load-carrying capacity of composite angle structures.

CHAPTER III

CLOSED-FORM SOLUTION EQUATIONS

There are two main equations used within the ASTM D6415 standard to calculate the maximum radial stress, one that is an exact solution and one that can be used as an approximate simple calculation [2]. The exact solution was developed by Lekhnitskii [18] for the stresses in a curved beam segment with cylindrical anisotropy. The radial stress is given by Eq. 1, 2, 3, 4, and 5 for a curved beam under pure bending where σ_r is the radial stress, r_o and r_i are the outer and inner radius of the curved segment, respectively, r_m is the radial position of the maximum radial stress, and E_θ and E_r are the moduli in the tangential and radial directions, respectively. The standard states that because the segment is under pure bending, the radial stresses are independent of angular position.

$$\sigma_r = -\frac{CBS}{r_o^2 g}\left[1 - \frac{1-\rho^{k+1}}{1-\rho^{2k}}\left(\frac{r_m}{r_o}\right)^{k-1} - \frac{1-\rho^{k-1}}{1-\rho^{2k}}\rho^{k+1}\left(\frac{r_o}{r_m}\right)^{k+1}\right] \tag{1}$$

$$g = \frac{1-\rho^2}{2} - \frac{k}{k+1}\frac{\left(1-\rho^{k+1}\right)^2}{1-\rho^{2k}} + \frac{k\rho^2}{k-1}\frac{\left(1-\rho^{k-1}\right)^2}{1-\rho^{2k}} \tag{2}$$

$$k = \sqrt{\frac{E_\theta}{E_r}} \tag{3}$$

$$\rho = \frac{r_i}{r_o} \tag{4}$$

$$r_m = \left[\frac{(1-\rho^{k-z})(k+1)(\rho r_o)^{k+z}}{(1-\rho^{k+z})(k-1)r_o^{-(k-z)}}\right]^{\frac{1}{2k}} \tag{5}$$

The curved beam strength (CBS) or moment per width is also necessary in calculating the radial stress. The curved beam strength can be calculated using Eq. 6, 7, and 8 where w is the width of the specimen, d_x is the horizontal distance between the two adjacent top loading bars of the load fixture, P is the total force at the first force drop (corresponding to the initial delamination), D is the diameter of the loading bars, t is the average thickness of the specimen, Φ is the angle from horizontal of the specimen legs, and Δ is the relative displacement between the top and bottom halves of the four-point-bending fixture[2].

$$\mathrm{CBS} = \frac{M}{w} = \frac{P_b l_o}{w} = \left(\frac{P}{2w\cos\phi}\right)\left(\frac{d_x}{\cos\phi} + (D+t)\tan\phi\right) \tag{6}$$

$$d_y = d_x \tan\phi_i + \frac{D+t}{\cos\phi_i} - \Delta \tag{7}$$

$$\phi = \sin^{-1}\left(\frac{-d_x(D+t)+d_y\sqrt{d_x^2+d_y^2-D^2-2Dt-t^2}}{d_x^2+d_y^2}\right) \tag{8}$$

The approximate simple calculation (Eq. 9) can be used to verify the stress calculated in Equation 1. The accuracy of the equation decreases as the E_θ/E_r ratio increases or the r_i/r_o ratio (ρ) decreases [2]. Equation 9 was referenced in ASTM D6415 from the Kedward, Wilson, and McLean text [3].

$$\sigma_r^{max} = \frac{3 \cdot CBS}{2t\sqrt{r_i r_o}} \tag{9}$$

The simplification of Equation 9 will be discussed following the introduction of the next two equations (Eq. 10 and 11).

The Kedward, Wilson, and McLean text also analyzes two other approximate equations which will be explored within this paper. The additional equations are Equation 10 and 11 [3]. The first approximate equation is

$$\sigma_{r,max} = \frac{3M}{2btR_m} \tag{10}$$

where R_m is the mean radius and the second approximate equation is

$$\sigma_{r,max} = \frac{12M}{bt^3}\left[R_m - (r_i r_o)^{\frac{1}{2}}\right]. \tag{11}$$

Both equations are derived using simple bending theory (i.e. a linear distribution of circumferential stress is assumed). The basic difference in the respective derivations is that Equation 10 assumes that the radial stress at the central plane ($r = R_m$) is the maximum value, while Equation 11 solve for the correct radial location ($r = (r_i r_o)^{1/2}$) at which the maximum σ_r exists, consistent with the linear σ_θ assumption. The major error in Equation 10 is due to solving for $\sigma_{r,max}$ at the incorrect radial location. Kedward, Wilson, and McLean modified this equation to give a significantly improved estimate simply by substituting the correct value ($r = (r_i r_o)^{1/2}$) used in Equation 11. The resulting equation is the approximate equation used in the ASTM D6415 standard, Equation 9.

CHAPTER IV

FINITE ELEMENT ANALYSIS

The bracket has been analyzed for this study using the ABAQUS finite element program [19]. The model is fully three-dimensional, using linear-displacement 8-node brick elements (type C3D8) [19].

The first model created was for Bracket A, as seen in Table 1. This bracket has 8 plies, a 0.125 inch radius, and is made up of the base material. Multiple runs were made on the first model to ensure that it was working properly and the results were converging (mesh refinement). After successfully creating this first model, the material properties were changed to those with nano-modified resin (NMR). The same type of process was performed for each type of bracket with and without NMR. The variables of each of the specimen, A through H, can be seen in Table 1.

The composite material properties and references needed for the material database within ABAQUS are located in Table 2. It was important to assign these material properties to the models of the brackets within ABAQUS, so that the warp and fill directions (designated "1" and "2," respectively) were running along the length or width of the composite, and that the 3-direction was correctly positioned to run through the thickness. In order to do this, the material

TABLE 1. TEST MATRIX				
Specimen Type	Radius	# of Plies	NMR	# of Specimen
A	0.125"	8	Yes	3
B	0.125"	8	No	3
C	0.125"	16	Yes	3
D	0.125"	16	No	3
E	0.25"	8	Yes	3
F	0.25"	8	No	3
G	0.25"	16	Yes	3
H	0.25"	16	No	3

TABLE 2. MATERIAL PROPERTIES					
	AS4 5HS Carbon 862/W Epoxy	Reference		AS4 5HS Carbon 862/W Epoxy w/ PR-24-XT-OX Nano	Reference
E_1(Msi)	9.24	D3039 [20]	E_1(Msi)	9.55	D3039 [20]
E_2(Msi)	8.40	D3039 [20]	E_2(Msi)	9.37	D3039 [20]
E_3(Msi)	1.50	Kim [22]	E_3(Msi)	1.65	Kim [22]
G_{12}(Msi)	0.61	D3518 [21]	G_{12}(Msi)	0.60	D3518 [21]
G_{13}(Msi)	0.74	Daniel & Ishai [1]	G_{13}(Msi)	0.60	Kim [22]
G_{23}(Msi)	0.59	Daniel & Ishai [1]	G_{23}(Msi)	0.60	Kim [22]
v_{12}	0.05	D3039 [20]	v_{12}	0.04	D3039 [20]
v_{21}	0.045	D3039 [20]	v_{21}	0.05	D3039 [20]
v_{13}	0.50	Daniel & Ishai [1]	v_{13}	0.50	Kim [22]
v_{23}	0.37	Daniel & Ishai [1]	v_{23}	0.37	Kim [22]

orientation needed to be correctly assigned to the bracket. First, datum planes were created at the point where the leg and the radius meet, for both the left and right legs of the bracket. This can be seen in Figure 1. The datum planes are the dashed lines intersecting the bracket. The datum planes were then used to partition the cells of the bracket. As a result, the cells of the left leg, right leg, and radius were able to be treated separately. After partitioning the cells, local coordinate systems were created for each segment of the bracket. A rectangular coordinate system (X-, Y-, and Z-axes) was assigned to the left and right leg of the model, while a cylindrical coordinate system (R-, T-, and Z-axes) was assigned to the radius. The coordinate systems can also be seen in Figure 1. Notice that the X-direction of both legs and R-direction of the radius are actually running through-the-thickness of the bracket (in the global Y-direction). It should be noted that when applying the material orientation, 90° rotations about the local Y- and T- axes of the systems were made, so that the resulting directions of the material properties were as follows: X-direction running along the width of the bracket, Y-direction along the length of the bracket, and Z-direction through-the-thickness of the bracket. The same applies for the cylindrical coordinates. Because this rotation caused the X- and R-direction of the coordinate system to run along the width and the Y- and T-direction of the coordinate system to run along the length of the bracket (opposite of the material orientation of the actual brackets), the material properties were simply interchanged. For example, in the material database, the actual value for E1 was entered into the cell for E2 (in

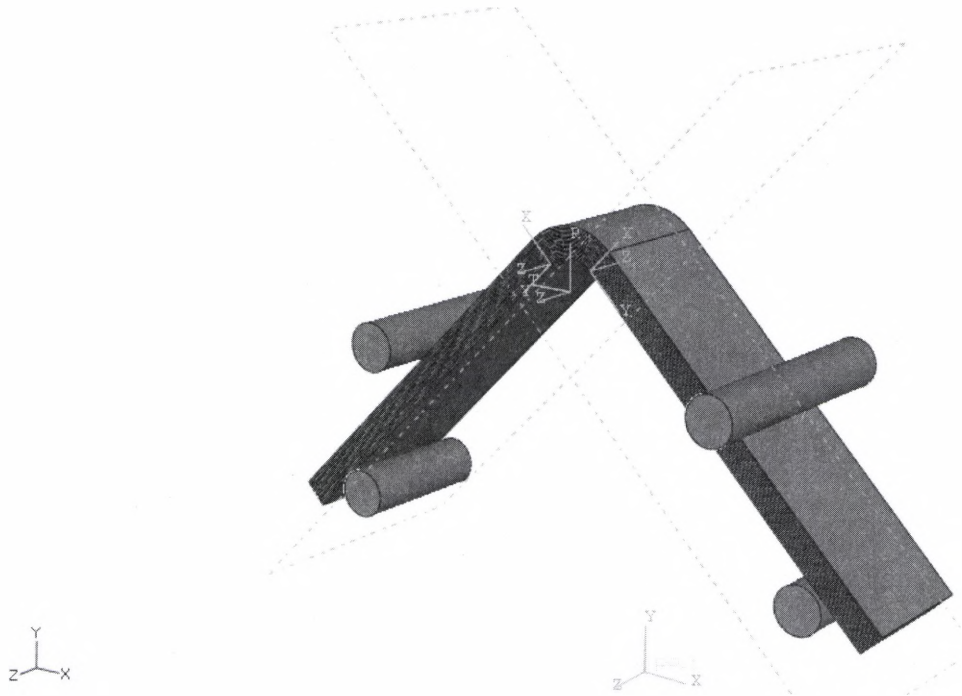

Figure 1. ABAQUS Model Layout

ABAQUS). This was done for all of the material properties (v_{12}, v_{21}, etc.) so that everything was able to be correctly modeled.

The loading arms used in the four-point bend test for ASTM D6415 standard were also modeled for the finite element analysis. Both the top and bottom loading bars were created and positioned using the dimensions in the standard. The loading arms and surfaces of the bracket were modeled as a surface-to-surface contact problem in ABAQUS. It was necessary to assign a "slave" surface and "master" surface to the parts interacting during contact. All loading bars were assigned "slave" surfaces and given a finer mesh and the top and bottom surfaces of the right and left leg of the bracket were assigned "master" surfaces.

Initially, a positive load of 100 lb in the Y-direction was applied to the bottom loading bars using a reference point which can be seen in Figure 1. A load of 100 lb was chosen so that it could be easily scaled to match the maximum experimental load experienced by the bracket at the first load drop. After scaling the load to the experimental value, the stresses were then scaled too. This technique was not used for brackets that experienced a load greater than 200 lb due to the non-linearity of the problem caused by flexure in the legs of the composite angle bracket. Determination of the 200 lb cutoff point will be discussed later. A separate job analysis was run in ABAQUS, using the exact failure load experienced by each bracket, in order to produce the exact stress. The bottom loading bars were also given boundary conditions to suppress all

movement in the X- and Z- directions. Boundary conditions for the top loading bars eliminated movement in all directions.

Various meshes were tested on the models in order to ensure that the results were converging. The first model created was for Bracket A. It contained 9 elements along the radius, 1 element per ply, 30 elements along the width, and 30 elements down the legs. Edge biasing was used in ABAQUS for the elements running down the length of the legs. This allowed for a coarser mesh towards to the bottom of the legs and a finer mesh towards the top of the legs. The bias value was set at 10, which produced an even transition between the mesh of the legs and the mesh of the radius. The maximum though-the-thickness tensile stress value for this particular mesh at an applied load of 100 lb was determined and then compared to the other meshes.

Figure 2 shows a mesh refinement for one of the angle brackets. The only segment of the mesh that was varied during this process was the number of elements along the radius of the angle bracket. Looking at the figure, it can be seen that the difference in the maximum stress values from the first to second mesh was 1.0 percent, second to third was 0.45 percent, and so on, until the difference between the last two meshes decreased to 0.09 percent. This same approach was used for each type of bracket modeled.

It should be noted that a new mesh refinement study would be required if multi-directional laminates were introduced, and high accuracy was required for the interlaminar stresses.

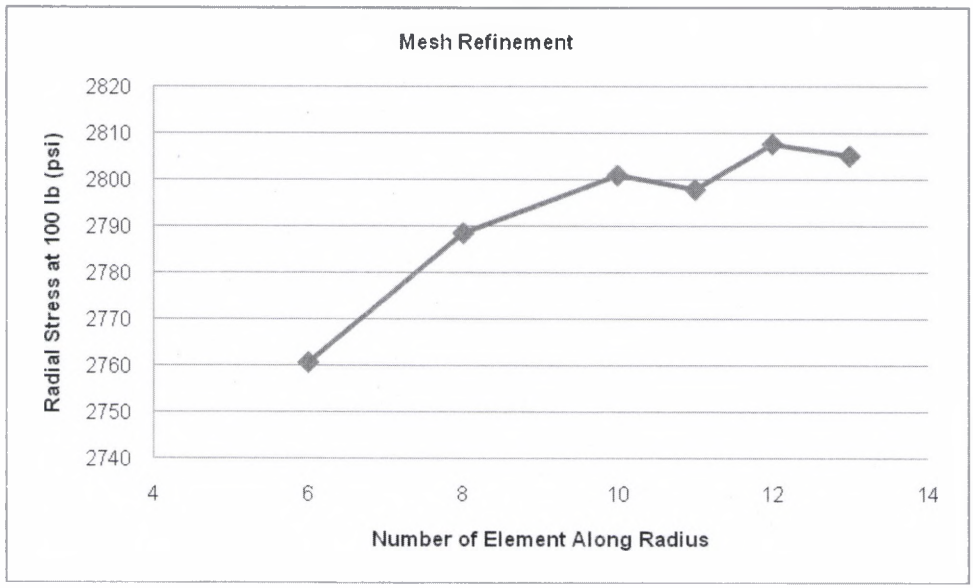

Figure 2. Mesh Study of Models Used in ABAQUS

While running the analysis of the first composite bracket modeled, other changes were made to the default settings to improve accuracy and reliability. In the step module, the initial increment size was decreased to values of 0.1, 0.01, and 0.001, depending on the job. The minimum increment size was also decreased to 1E-009 and the maximum number of increments was increased to 500. The final change made was to the time increment value (I_A) which controls the number of allowable attempts for each increment. This value was also increased to 20.

CHAPTER V

TEST MATRIX, SPECIMEN PREPARATION, AND MATERIAL PROPERTIES

Test Matrix

The variables under consideration included the curved beam radius, ply count (thickness), and addition of nano-modified resin (NMR), as seen in Table 1. The specimens tested had radii of 0.125 inches and 0.25 inches (0.25 inches is recommended in ASTM D6415 [2].) The laminate thicknesses were 0.112 inches (8 ply) and 0.224 inches (16 ply), both within the limits of 0.08 to 0.50 inches recommended in ASTM D6415 [2].

Specimen Preparation

The base material used for the composite was Hexcel AS4 intermediate modulus carbon five-harness satin weave and Epon 862/Epikure W epoxy resin. This composite was tested and compared to the composite with the NMR. The modified composite contained 10 grams per square meter (gsm) of Applied Sciences, Inc. PR-24-XT-OX vapor grown carbon nanofiber in chemically staged Epon 862/Epikure W epoxy resin; therefore, there was 80 gsm of the nanofiber in the 8-ply composite and 160 gsm of the nanofiber in the 16-ply composite. The nanofibers were dispersed into the resin by shear mixing. The process used has

been proven to distribute the nanofibers throughout the resin without clumping, ensuring that the fibers were well dispersed within the resin and film before infusion into the fiber preform [23, 24]. The abbreviation PR-24 refers to the amount of chemical vapor deposition (CVD) carbon on the surface [23, 24]. XT refers to the extra low density of the nanofiber (between 1.0-2.0 lb/ft^3), and OX refers to the functionalization, this one being oxygen functionalized. The gsm designation is the amount of nanofiber applied to neat resin films used in the resin film infusion process. The amount of carbon nanofiber loading was selected based on a balance of processability and previously demonstrated property improvements.

The resin described was chemically staged. This indicates that the Epon 862 was cured with the required 22.5 percent of Epikure W for two hours at 250°F. A percentage of 22.5 of Epikure W was used so that cross linking would not occur [23, 24]. An amount greater than 50 percent would theoretically cause cross linking to take place. The curing process caused the primary amines to react, which then lengthened the polymer chains. The longer polymer chains caused the viscosity to increase. The purpose of increasing the viscosity was to make it possible to film the resin and work with it to lay up on panels.

Sheets of the fiber and resin were laid up by hand on a male tool with the appropriate radius as shown in Figure 3. The original bracket panels were made to be 24 inches by 24 inches. At first, a caul plate was used to cover the plies of the bracket panel that were laid up on the tool. Later, a rubber layer (1/32 inches

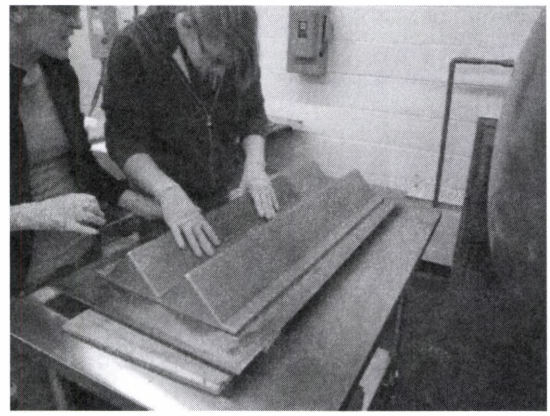

Figure 3. Layup of Composite Angle Bracket Panel

thick) was used because it was discovered that the rigid caul plate, if not matched exactly to the tool radius and laminate thickness, applied too high a pressure to the material at the critical radius, causing a thickness variation around the radius. After covering the plies with the rubber layer, the tool and the material were then vacuum bagged, and prepared for the autoclave. The brackets were cured under full vacuum and 100 psi autoclave pressure to ensure that the bag was fully sealed and there were no leaks. They were then heated to 250°F at 5°F/min, held for two hours, heated up to 350°F at 5°F/min, held for another two hours, and finally, allowed to cool to room temperature at a rate of 10°F/min.

It should be noted that when curing the composite, the nanofiber tended to be filtered out by the fabric and remain between the plies [23, 24]. This caused minimal penetration of the nanofiber into the tows and a higher concentration of the nanofibers in the resin between the plies [23, 24].

When the bracket panels were removed from the autoclave and tool, they were then cut into specimens using a diamond saw. After being machined, the specimen edges were sanded in order to meet the stated specimen geometry. The dimensions of the specimen can be seen in Figure 4. The width of the specimen was 1.0 inch, while the length of each leg was 3.5 inches. All dimensions were measured and recorded using calipers and a micrometer. It should also be noted that multiple measurements were taken of each specimen per the requirements of ASTM D6415 [2]. A total of five widths and five thicknesses were measured; three widths around the radius were taken and two widths on each leg (the same applied for the thicknesses). An average value of the three widths around the radius and an average value of the two widths on the legs were calculated. The same technique was used for the thicknesses.

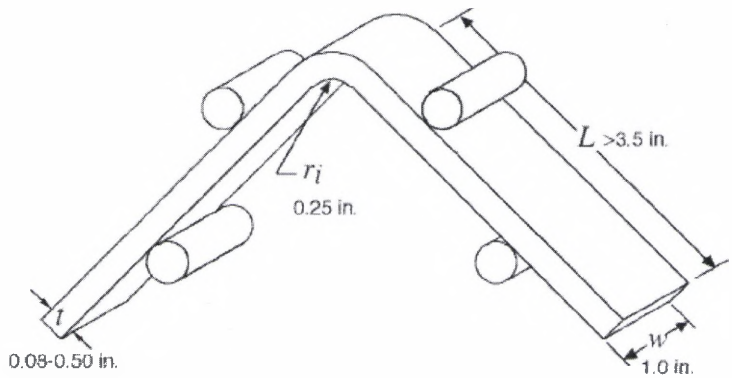

Figure 4. Dimensions of ASTM 6415 Curved Beam Strength Specimen [2]

The edges of one of each different type of specimen were given a fine polish so that micrograph photos could be taken. Photomicrographs were taken both before and after load testing for comparison.

After fabrication, the specimens were stored under ambient laboratory conditions until tested (less than two weeks).

Material Properties

Flat panels of the bracket material under consideration were fabricated and tested in order to acquire appropriate material properties needed for radial stress calculations and finite element analysis. Three different types of panels were created for the ASTM D3039 – 00 (Standard Test Method for Tensile Properties of Polymer Matrix Composite Materials) [20] and ASTM 3518 - 94 (Standard Test Method for In-Plane Shear Response of Polymer Matrix Composite Materials by Tensile Test of a ± 45° Laminate) tests [21]. Panels were made for the material both with and without the NMR.

The first type of panel was cut so that the fibers running in the weft direction of the weave were along the longitudinal length of the specimen. The next panel was cut so that the fibers running in the fill direction of the weave were along the longitudinal length of the specimen. Each of these panels were machined for the ASTM 3039 tension test in order to get the moduli, E_1 and E_2, and Poisson's ratios, v_{12} and v_{21}. The final panel was made for the ASTM 3518 tension test with the fibers in the fill and weft directions running in the ± 45°

direction. These specimens were tested in order to obtain the shear chord modulus G_{12}.

A total of five specimens were used for each of the ASTM tests. Results for the properties can be seen in Table 3 for the material with and without NMR.

TABLE 3. FLAT PANEL MATERIAL PROPERTIES MEASURED FOR THIS STUDY

	Without NMR	With NMR
E_1 (Msi)	9.24 ± 0.36	9.55 ± 0.31
E_2 (Msi)	8.40 ± 0.37	9.37 ± 0.22
ν_{12}	0.05 ± 0.02	0.04 ± 0.02
ν_{21}	0.04 ± 0.01	0.05 ± 0.002
G_{12} (Msi)	0.61 ± 0.01	0.60 ± 0.01

CHAPTER VI

EXPERIMENTAL SETUP AND PROCEDURE

The four-point-bend test apparatus can be seen in Figures 4, 5, and 6. The fixture follows all requirements of the ASTM D6415 standard. The cylindrical loading bars have diameters of 0.375 inches. The distance between the centerlines of the bottom loading bars is 4.0 inches, and the distance between the centerlines of the top loading bars is 3.0 inches.

The specimens were tested in an MTS servo-hydraulic load frame using displacement control. The tests were performed in ambient laboratory conditions (typically 72°F and less than 50 percent relative humidity).

In order to perform the test, the four-point bend fixture was properly mounted and aligned in the testing machine, so that the loading bars were all parallel to each other. Each specimen was placed between the top and bottom parts of the fixture, and roughly aligned in the center. Due to the geometry of the fixture and specimen, the specimen automatically centered itself between the loading bars when the force was applied. The suggested standard head displacement rate of 0.02 inches/minute stated in the ASTM standard was followed [2]. Data recorded while using the MTS load frame included the axial displacement of the crosshead, and the axial force. The specimen was

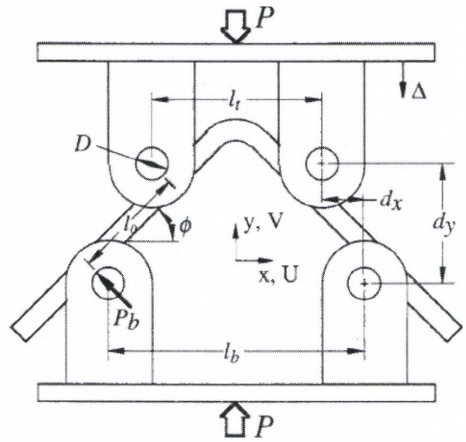

Figure 5. Curved Beam in Four-Point Bending [2]

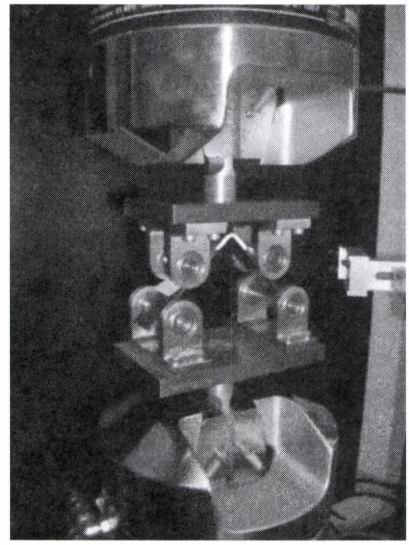

Figure 6. Loading Fixture and Specimen in MTS Servo-Hydraulic Load Frame

monitored, and the test was terminated once the load drop was half that of the peak force. All edges of specimen that were not used for micrographs were painted with a brittle white paint so that the failure mode could be more easily monitored.

CHAPTER VII

RESULTS AND DISCUSSION

A total of three specimens of each type of bracket listed in Table 1 were tested using the four-point bend test according to ASTM D6415. The experimental results examined included the maximum load experienced by each specimen, the curved beam strength (Eq. 6), and the maximum radial stress at initial failure (Eq. 1). The failure morphology of each specimen was observed using micrographs and the force-displacement graphs. All results were compared to finite element data obtained through the use of ABAQUS. Results were not used for two of the specimens due to fabrication flaws around the radius. Both specimens had a variation in the thickness and produced results that were misleading.

The maximum load experienced by each specimen can be seen in Figure 7. The data represent the mean value of three specimens at each configuration and the range from the minimum to the maximum indicated by the vertical bars. The brackets that retained the lowest level of load were the 8-ply 0.125-inch radius specimens with and without NMR. The average load was approximately 100 lb. The highest load retained was approximately 300 lb, experienced by the

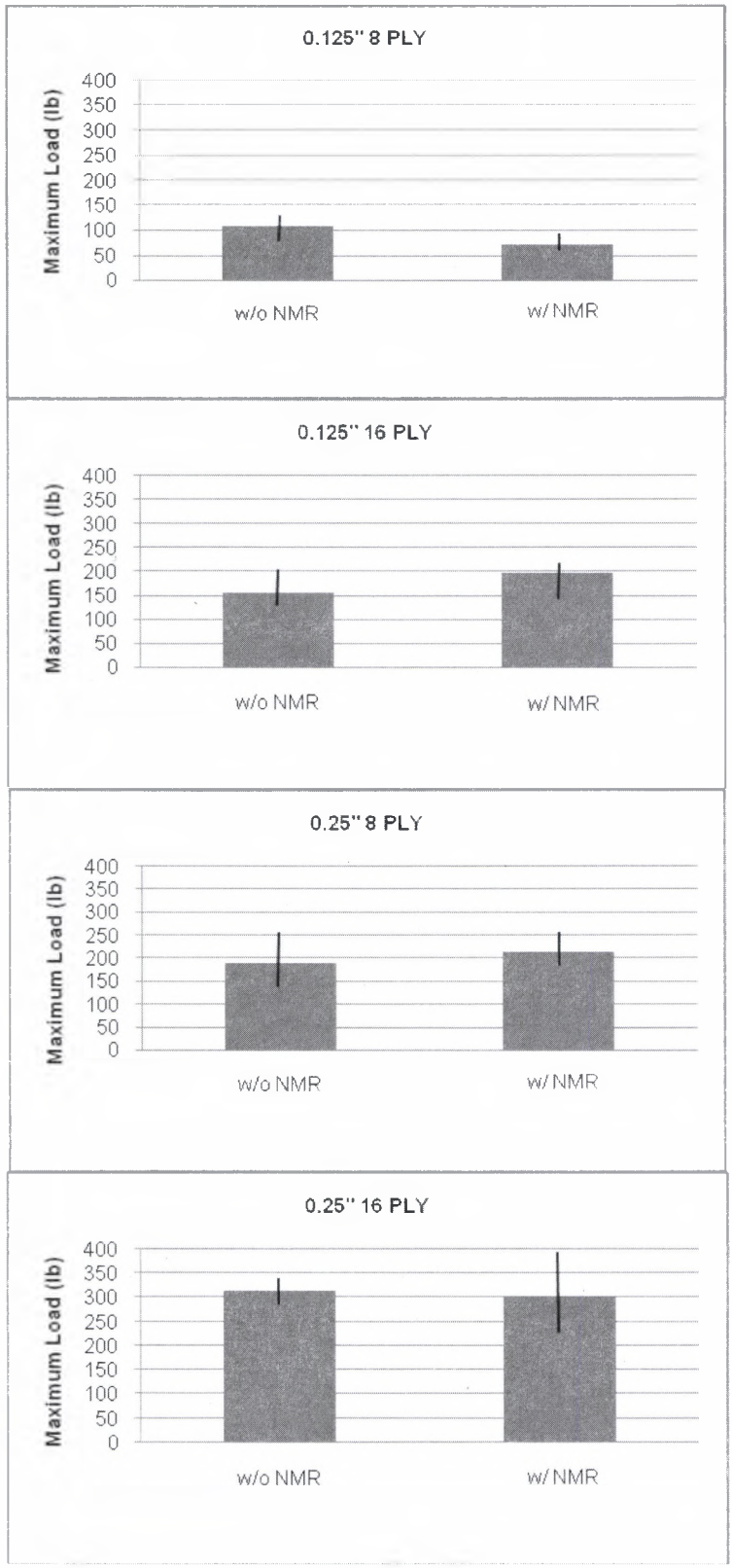

Figure 7. Maximum Load at Failure Initiation

16-ply 0.25-inch radius specimens with and without NMR. The addition of NMR for the 8-ply 0.125-inch radius specimens slightly decreased the maximum load that it was able to hold, while it increased the maximum load for the 16-ply 0.125-inch radius specimens. The maximum loads experienced by the 0.25-inch radius specimens all remained approximately the same with and without the NMR. In order to see the effects of the different variables on the maximum load, graphs were made comparing the maximum load of 0.125- and 0.25-inch radius specimens, 8- and 16-ply specimens, and with and without NMR specimens, as seen in Figure 8. When comparing the maximum load for the 0.125-inch and 0.25-inch radius specimens, it can be seen that the 0.125-inch specimens were not able to sustain as high a load as the 0.25-inch specimens. As for the 8- versus 16-ply bracket, the 8-ply specimens were also not able to maintain as high a load as the 16-ply specimens. Finally, when examining the brackets with and without NMR, it can be seen that both graphs look similar, with no real conclusion able to be made.

The curved beam strengths (CBS) of the brackets, as defined by Eq. 6, are shown in Figure 9. The specimens with the lowest and highest curved beam strengths correlate to the specimens with the minimum and maximum loads. The brackets with the lowest strength, around 50 lb-in/in, were the 8-ply 0.125-inch radius specimens and the brackets with the highest strength, around 250 lb-in/in, were the 16-ply 0.25-inch radius specimens. It can be seen that the brackets that had the largest difference in curved beam strength were the 16-ply specimens

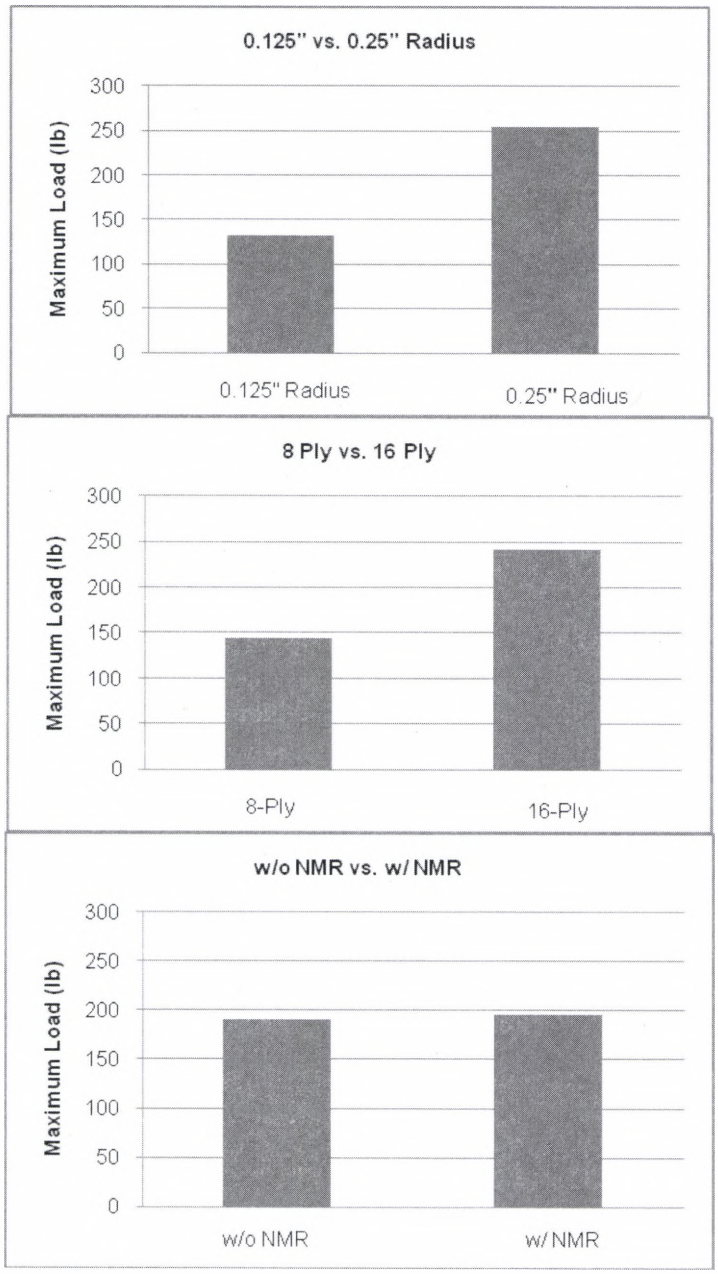

Figure 8. Variable Study for Maximum Load at Failure Initiation

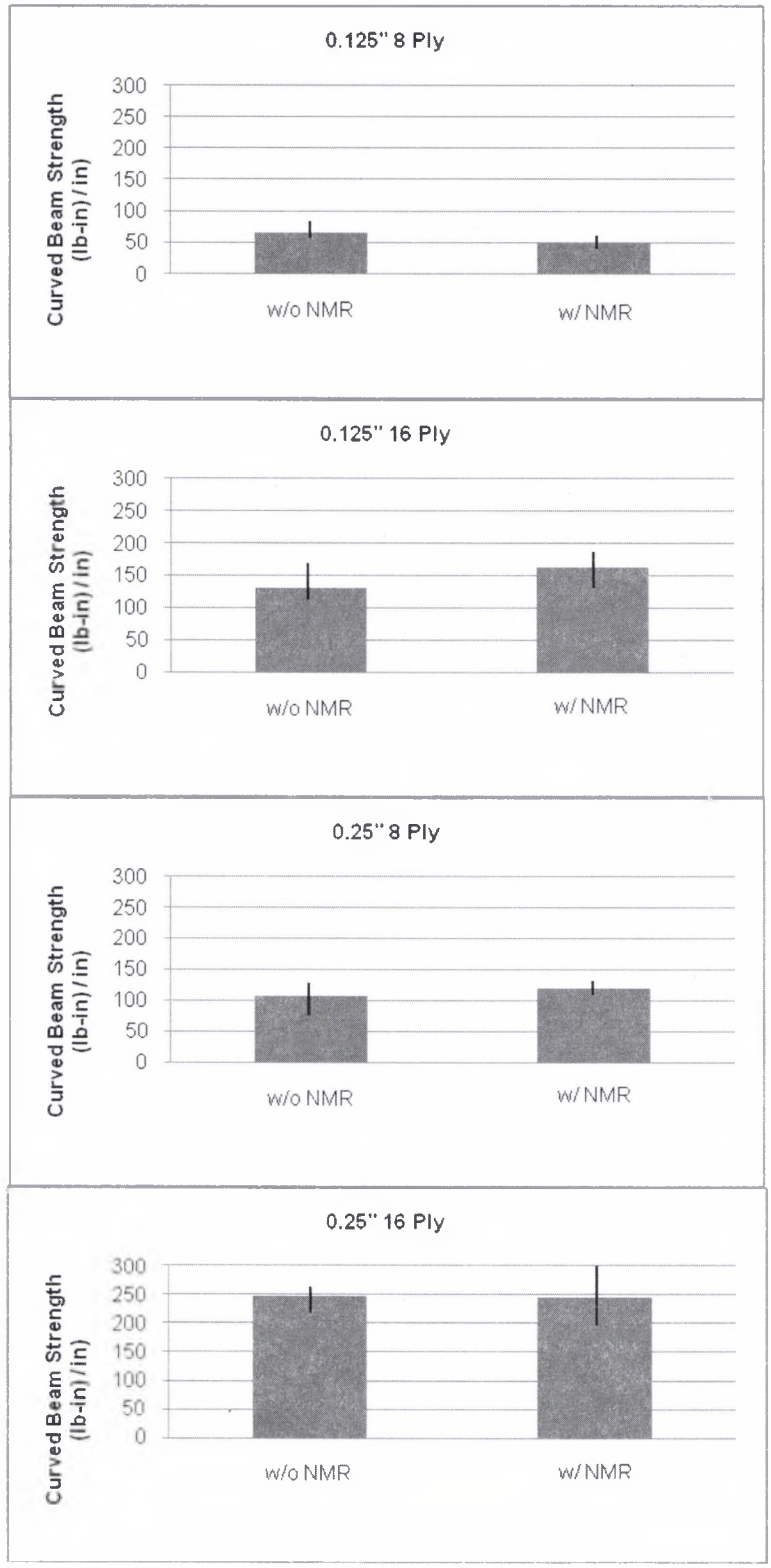

Figure 9. Curved Beam Strength

with the 0.125 inch radius. The strength increased approximately from 130, without NMR, to 165 lb-in/in, with NMR. A comparison between all variables was made for the curved beam strength in Figure 10. Once again, the effects of the NMR appeared to be not significant. The curved beam strength for the 16-ply brackets was higher than that of the 8-ply brackets, and the curved beam strength for the 0.25-inch radius specimens was higher than that of the 0.125-inch radius specimens.

To examine the effect of geometry (radius and thickness) and material properties, the radial stress at 100 lb load (independent of failure load) was calculated and compared, as shown in Figure 11. The three bars for each resin type correspond to the approximate equation, exact equation, and finite element analysis. Once again, the most extreme case is shown for the 8-ply brackets with the 0.125 inch radius. These specimens were subjected to the highest through-the-thickness stresses at 100 lb, with values near 4,200 psi. The brackets with the lowest radial stress at 100 lb were the 16-ply 0.25-inch radius specimens, with stress values near 1,500 psi. The NMR had the most effect on the radial stress of the 0.125-inch radius, 8-ply brackets. Stress values were shown to decrease by approximately 600 psi. There was a slight decrease in stress for the 16-ply 0.125-inch radius brackets, while there was little variation in stress for all 0.25-inch radius brackets. A difference in the radial stress can also be seen when comparing the brackets with the smaller and larger radii. The radial stress for the 0.125-inch brackets for the 8-ply specimens were almost double that of the 0.25-inch brackets for the 8-ply specimens. The same was true for the 16-ply

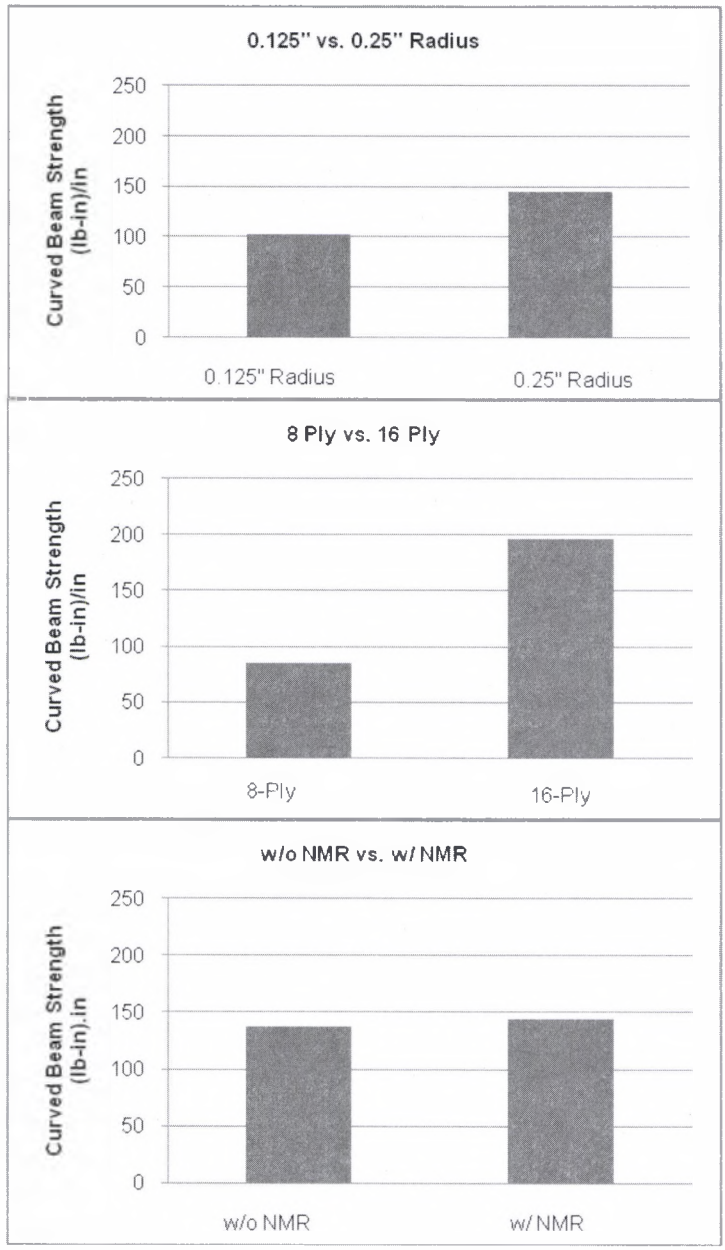

Figure 10. Variable Study for Curved Beam Strength

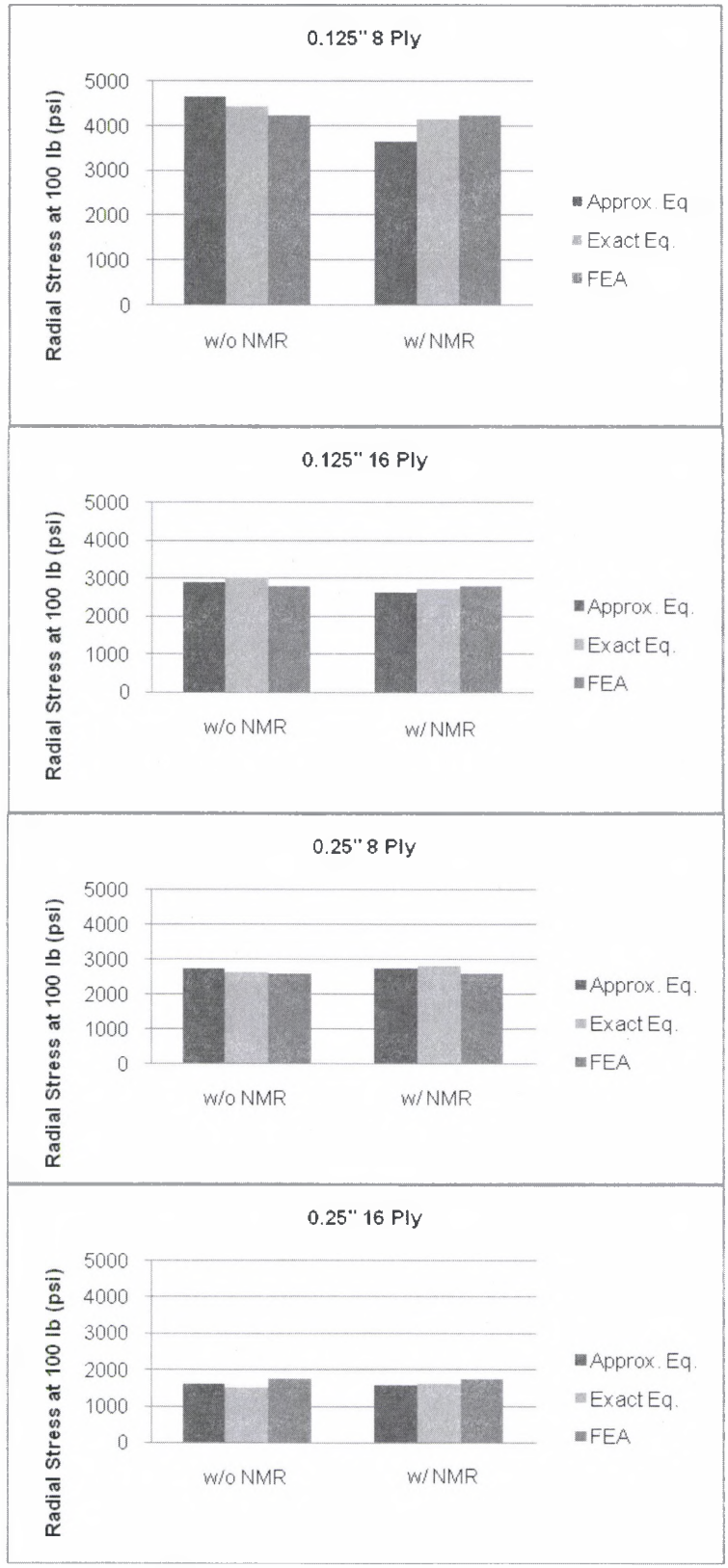

Figure 11. Calculated Radial Stress at 100 lb of Applied Load

specimens. Radial stress calculated from Eq. 1 and 9, the exact and approximate equations, produced similar results. These values were compared to the finite element analysis results obtained through the use of ABAQUS. The through-the-thickness stress was examined for each bracket at an applied load of 100 lb. The models can be seen in Figures 12 - 19.

The maximum radial stress at failure initiation can be seen in Figure 20 and Table 4. Stress values for all specimens tested are close to a 4,300 to 4,800 psi range, albeit with large scatter. Once again, the exact and approximate equations (Eq. 1 and Eq. 9), and finite element analysis were compared to each other. The ABAQUS model results for the radial stress due to an applied load of 100 lb, can be seen in Figure 12, for the 8-ply 0.25 inch radius specimen. The results for the other bracket models at an applied load of 100 lb can be seen in Figures 13 - 19. As previously stated, a resulting maximum stress value for the finite element analysis was determined by scaling the 100 lb load and corresponding stress, to the experimental load experienced by each bracket. This technique was not used for brackets that experienced a load greater than 200 lb due to the non-linearity of the problem caused by the flexure of the composite angle bracket legs. The determination of the 200 lb cutoff point was made by running multiple analyses in ABAQUS for 8- and 16-ply brackets. An analysis was run for the 8- and 16-ply brackets at a load of 100 lb, 200 lb, 300 lb, and 400lb, and the resulting maximum radial stress was determined. The stress value for the 100 lb load was then scaled accordingly for the 200 lb, 300 lb, and 400 lb loads. A comparison was then able to be made between the data obtained

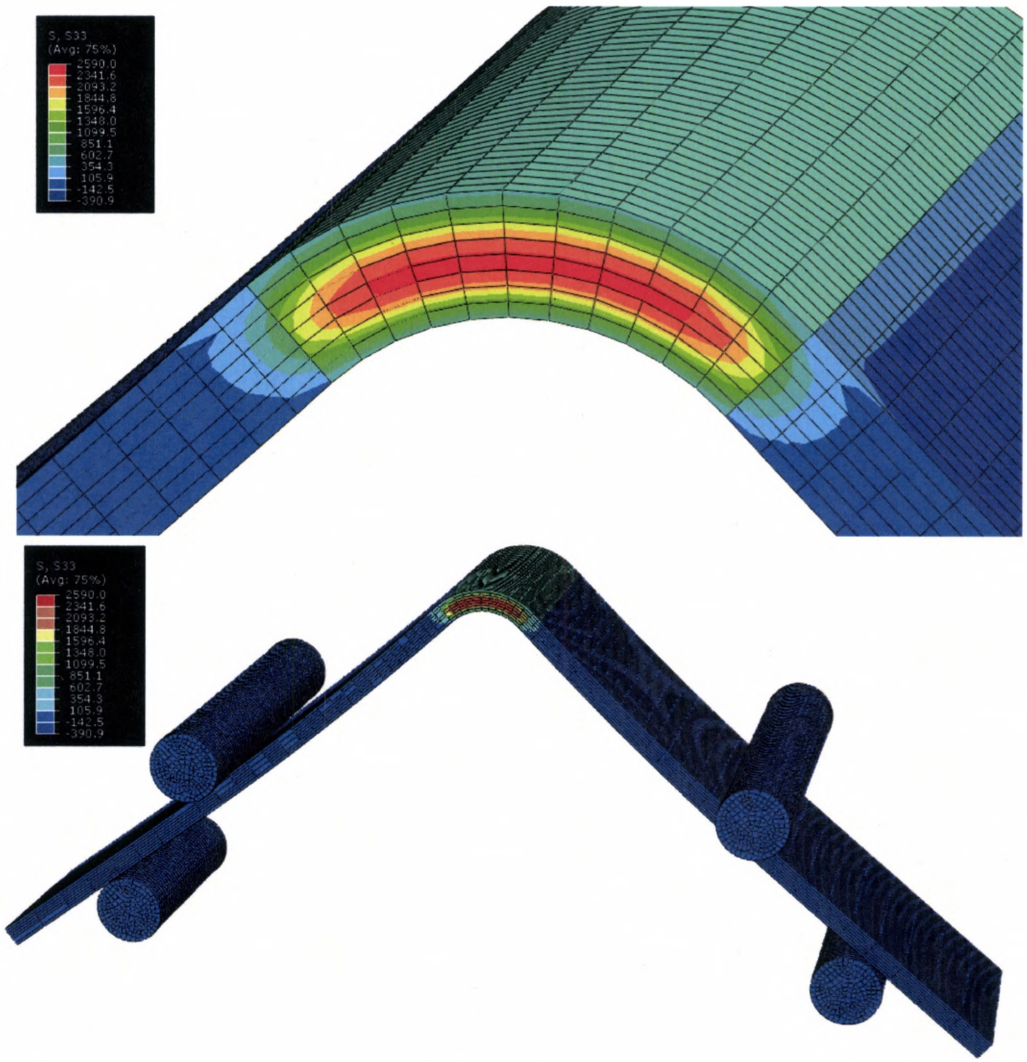

Figure 12. ABAQUS Results for the Through-the-Thickness Stress for 0.25" Radius 8-Ply Bracket Without NMR at Applied 100 lb Load

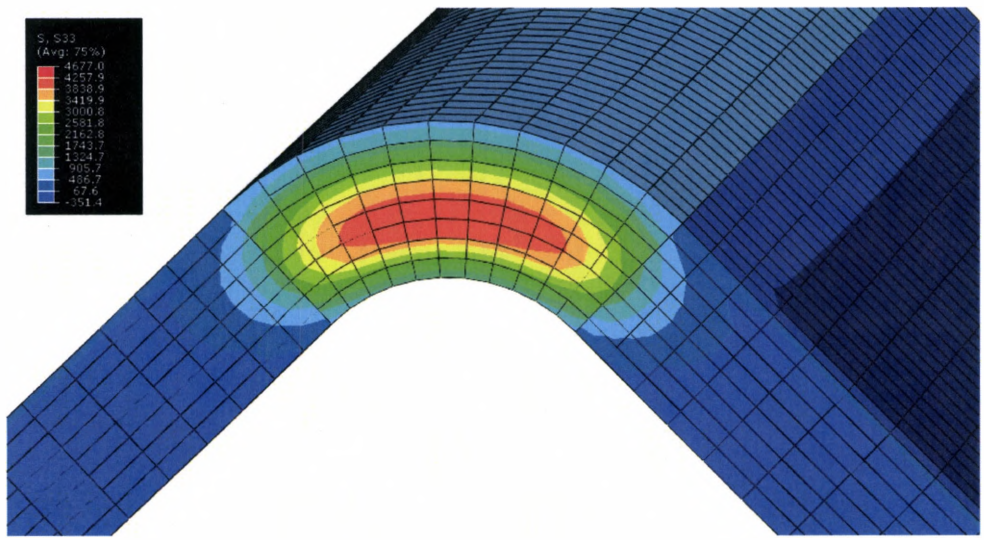

Figure 13. ABAQUS Results of Through-the-Thickness Stress for 0.125"-Radius 8-Ply Bracket Without NMR at Applied 100 lb Load

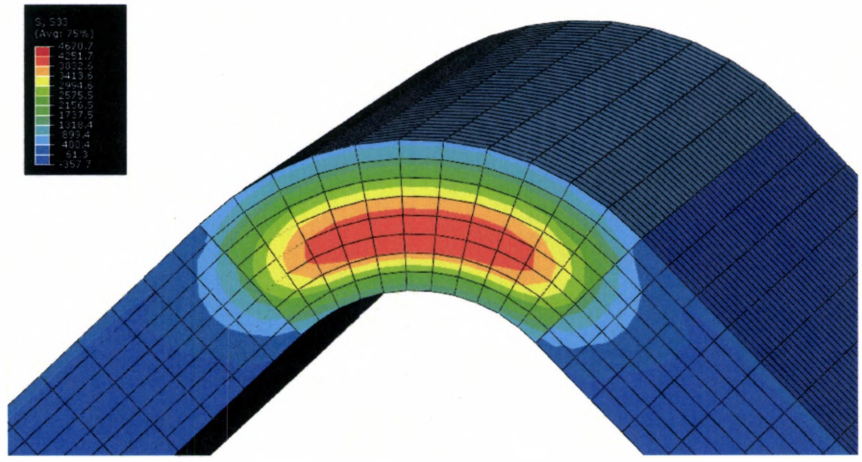

Figure 14. ABAQUS Results of Through-the-Thickness Stress for 0.125"-Radius 8-Ply Bracket With NMR at Applied 100 lb Load

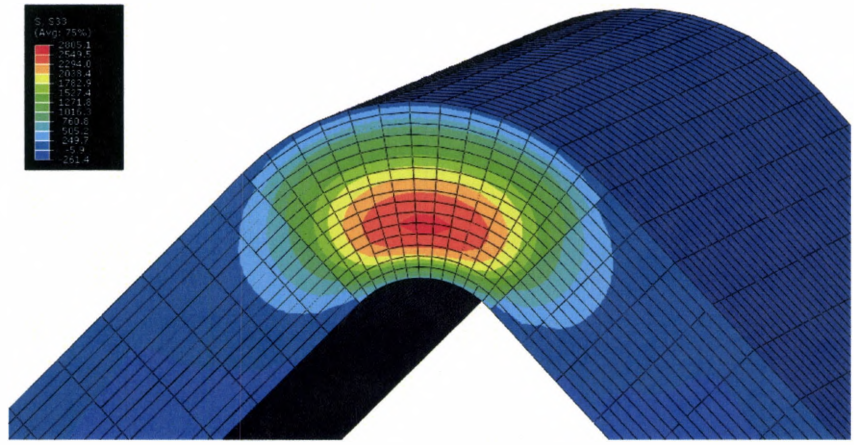

Figure 15. ABAQUS Results of Through-the-Thickness Stress for 0.125"-Radius 16-Ply Bracket Without NMR at Applied 100 lb Load

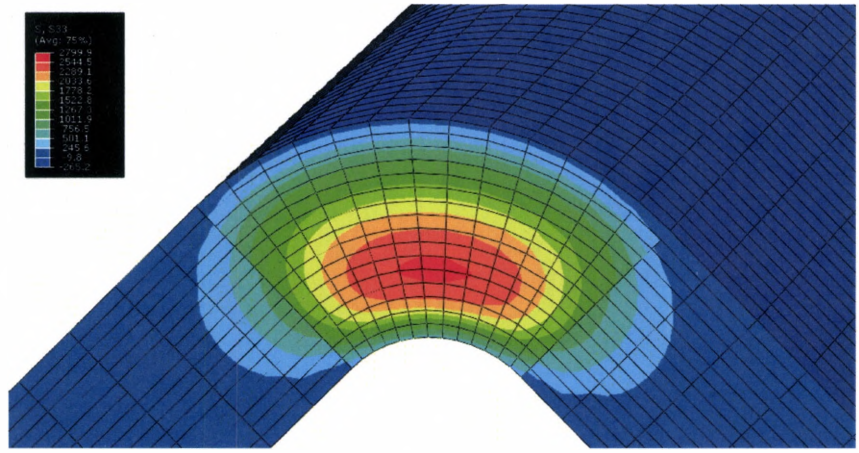

Figure 16. ABAQUS Results of Through-the-Thickness Stress for 0.125"-Radius 16-Ply Bracket With NMR at Applied 100 lb Load

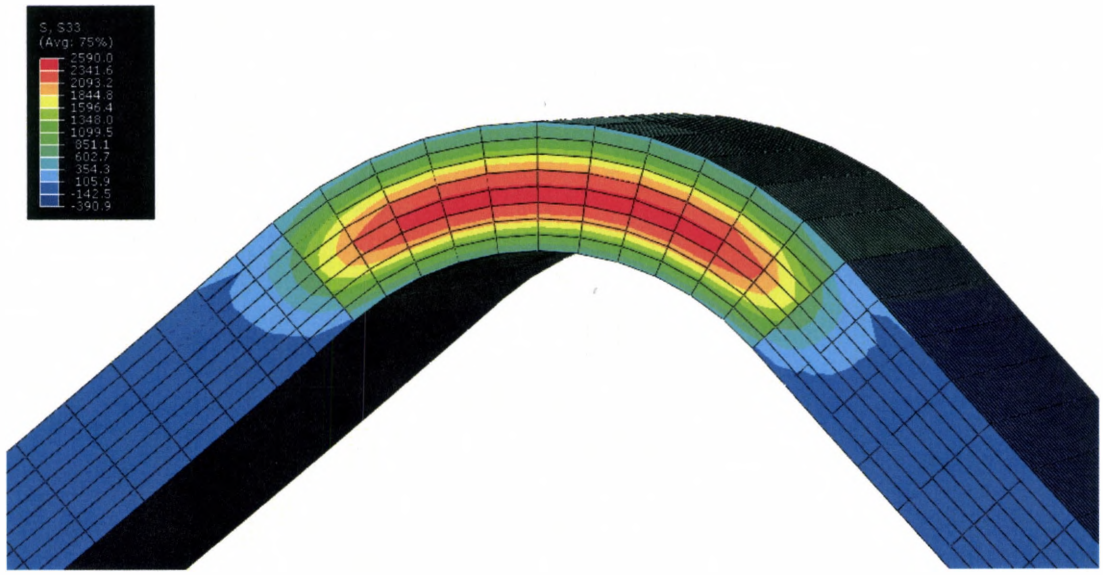

Figure 17. ABAQUS Results of Through-the-Thickness Stress for 0.25"-Radius 8-Ply Bracket With NMR at Applied 100 lb Load

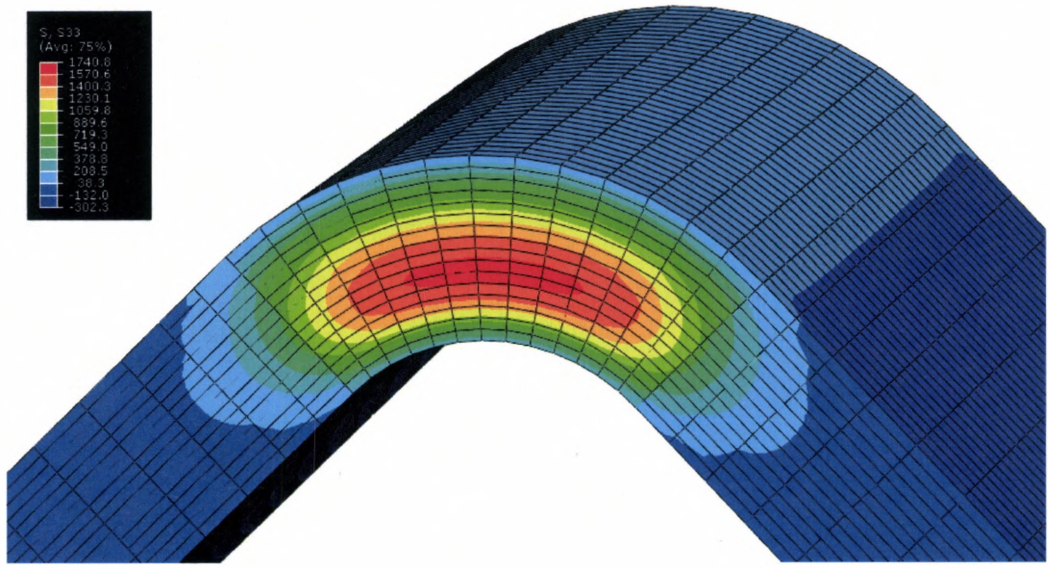

Figure 18. ABAQUS Results of Through-the-Thickness Stress for 0.25"-Radius 16-Ply Bracket Without NMR at Applied 100 lb Load

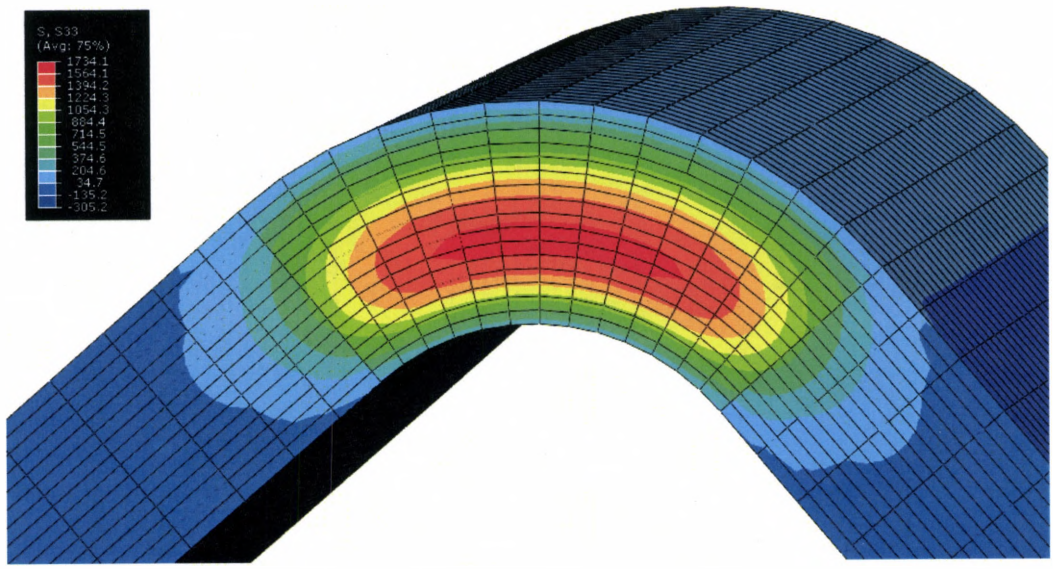

Figure 19. ABAQUS Results of Through-the-Thickness Stress for 0.25"-Radius 16-Ply Bracket With NMR at Applied 100 lb Load

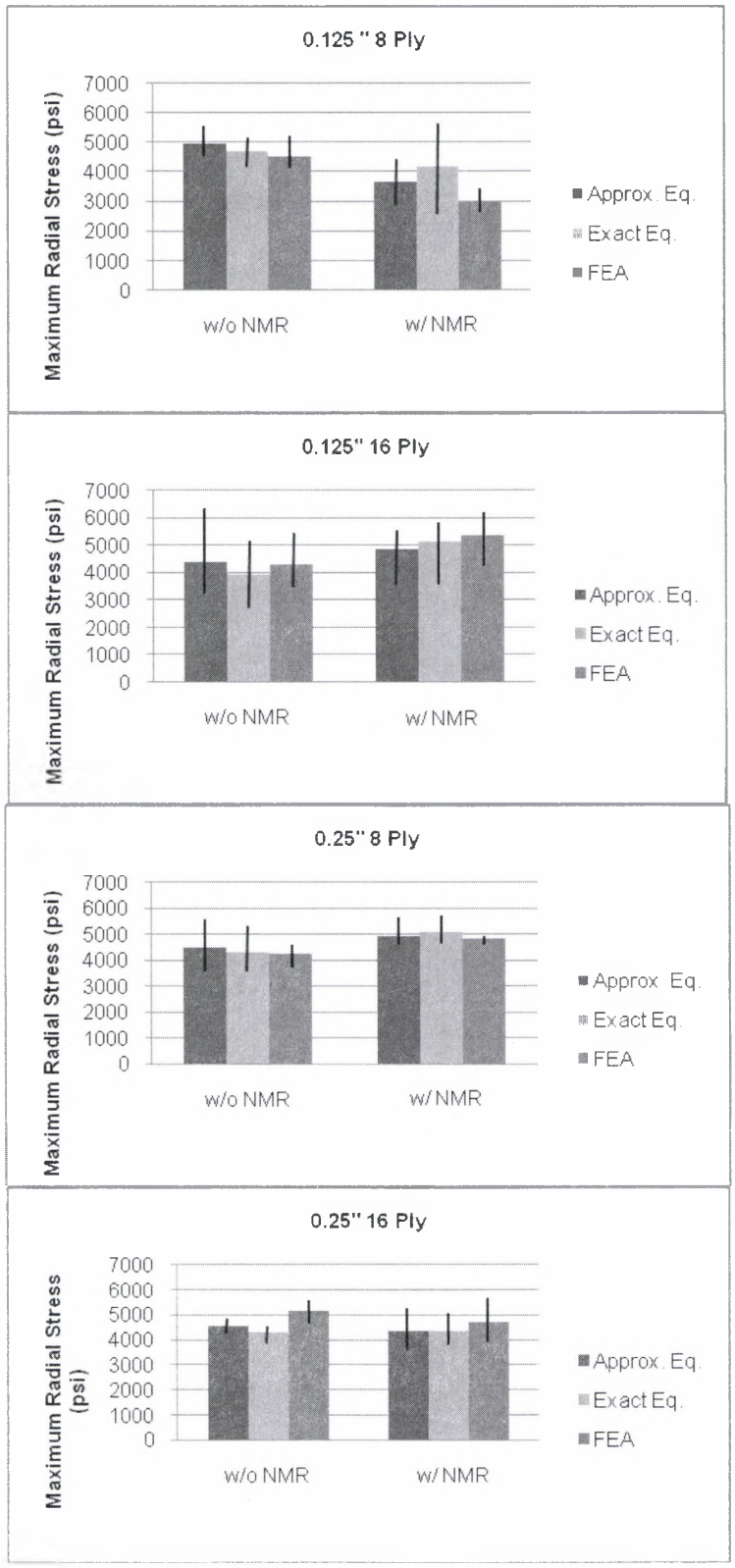

Figure 20. Maximum Radial Stress at Failure Initiation

TABLE 4. RADIAL STRESS AT FAILURE			
	Approx.	Exact	FEA
w/o NMR (ksi)	4.6 ± 0.88	4.3 ± 0.74	4.6 ± 0.70
w/ NMR (ksi)	4.5 ± 0.87	4.7 ± 1.05	4.5 ± 1.06

from the actual load in ABAQUS and the data acquired from extrapolation. Figures 21 shows the result for a 16-ply angle bracket. There is no error between the scaled value and actual value at 100 lb, 3.17 percent at 200 lb, 7.24 percent at 300 lb, and 21.9 percent at 400 lb. The cutoff of 200 lb was selected based on this percent error data; therefore, the extrapolated ABAQUS data lower than 200 lb has an error off less than 3.17 percent. The error for the 8-ply bracket at 200 lb was 5.88 percent and the error at 300 lb was 153.5 percent. The ABAQUS models that were run using the exact load can be seen in Figures 22 - 33.

The exact and approximate equations for the maximum radial stress were also plotted with respect to the finite element analysis data obtained from ABAQUS, so that a comparison could be made to see how well the analytical stress prediction correlated with the finite element stress prediction (Figures 34-35). Each data point on the graphs represent the ABAQUS value versus the exact equation value or approximate equation value for a specific specimen. The distance between the points and the line on the graph are representative of how well the analytical data correlated with the finite element analysis data. For example, points that are plotted closer to the line represent a specimen that had an analytical stress value that was very close to the finite element stress value. Data points were not plotted for the two specimens that had the thickness variation at the radius. By looking at each graph it can be concluded that the

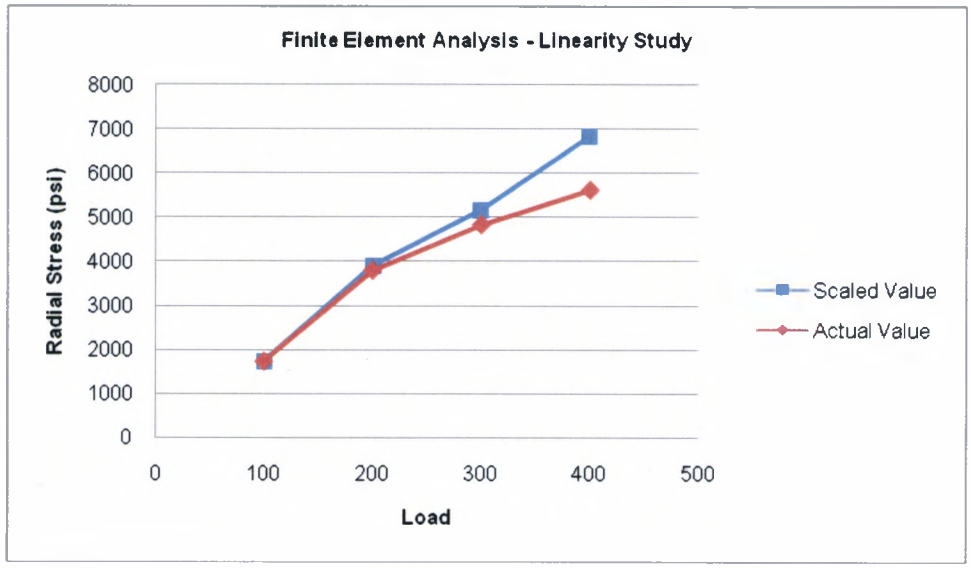

Figure 21. Linearity Study for Finite Element Analysis

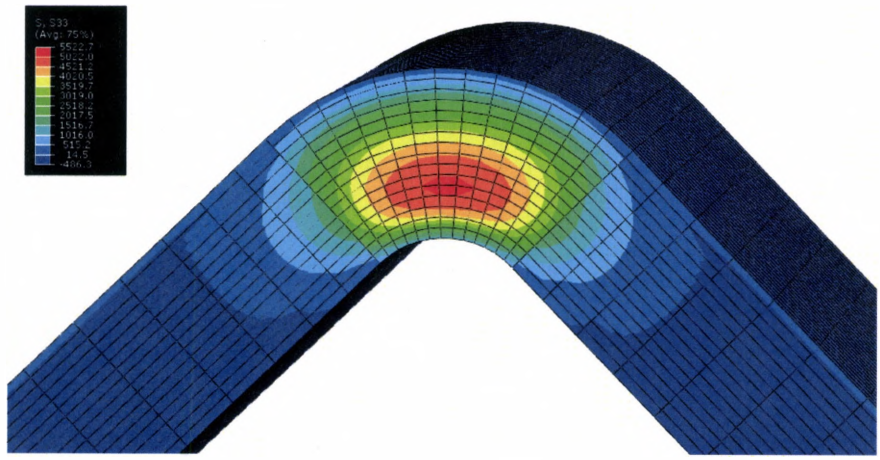

Figure 22. ABAQUS Results of Through-the-Thickness Stress for 0.125"-Radius 16-Ply Bracket Without NMR at 202.2 lb Load

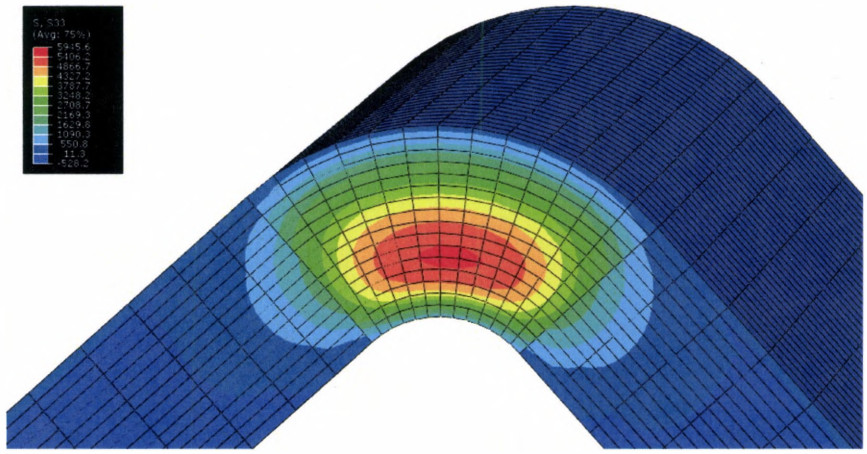

Figure 23. ABAQUS Results of Through-the-Thickness Stress for 0.125"-Radius 16-Ply Bracket With NMR at 218.8 lb Load

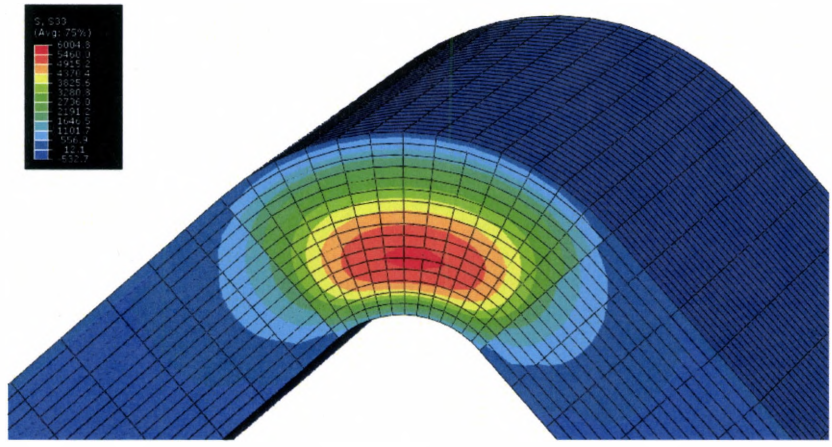

Figure 24. ABAQUS Results of Through-the-Thickness Stress for 0.125"-Radius 16-Ply Bracket With NMR at 221.1 lb Load

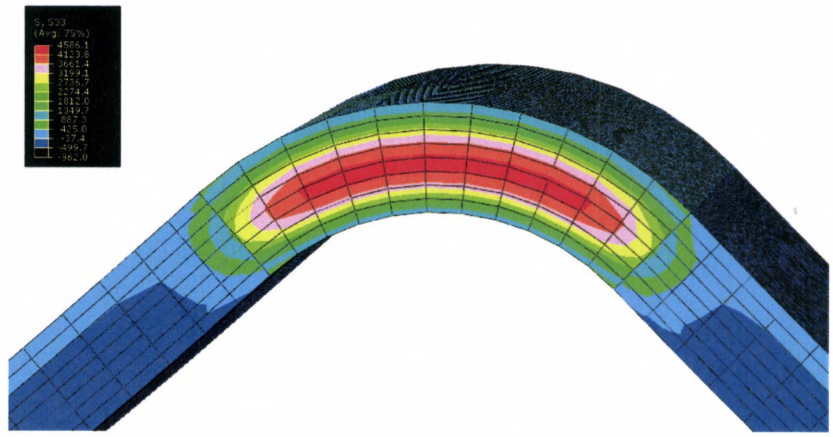

Figure 25. ABAQUS Results of Through-the-Thickness Stress for 0.25"-Radius 8-Ply Bracket With NMR at 250.6 lb Load

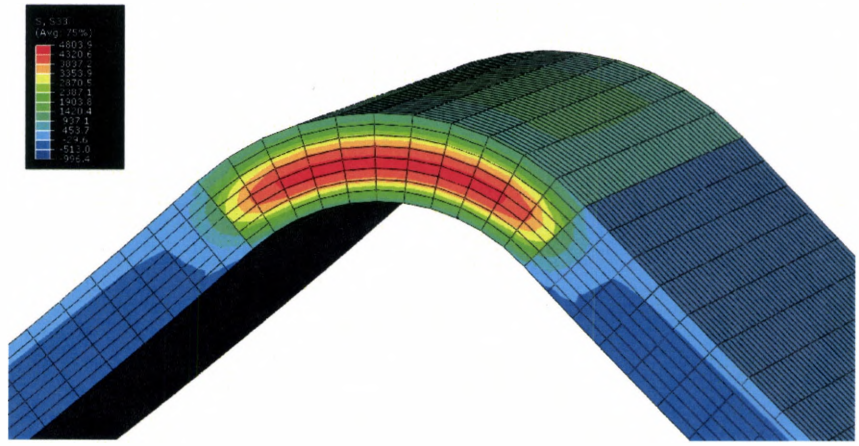

Figure 26. ABAQUS Results of Through-the-Thickness Stress for 0.25"-Radius 8-Ply Bracket With NMR at 253.6 lb Load

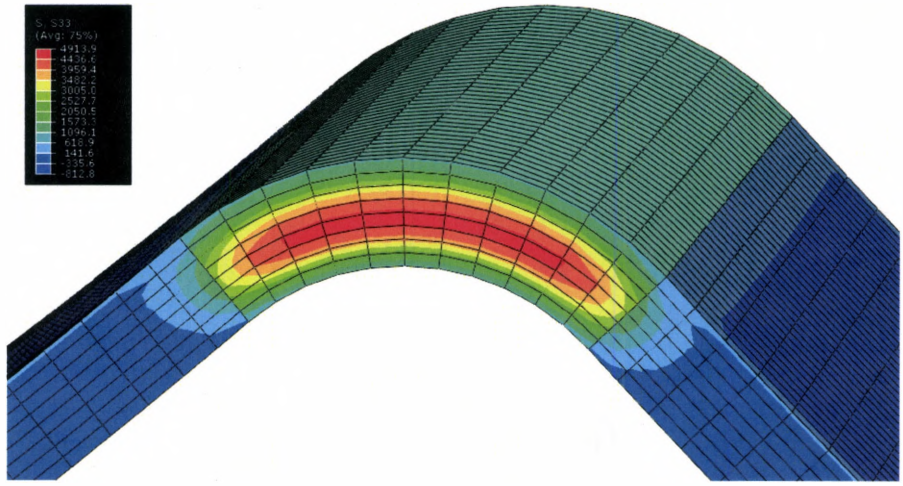

Figure 27. ABAQUS Results of Through-the-Thickness Stress for 0.25"-Radius 8-Ply Bracket With NMR at 206.5 lb Load

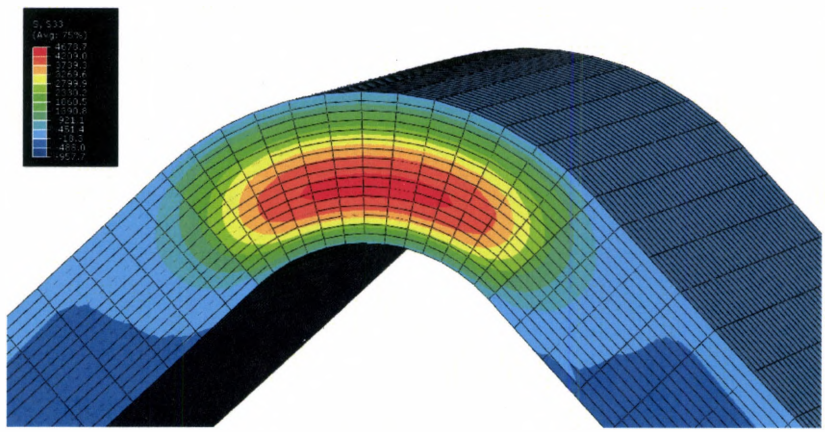

Figure 28. ABAQUS Results of Through-the-Thickness Stress for 0.25"-Radius 16-Ply Bracket Without NMR at 281.3 lb Load

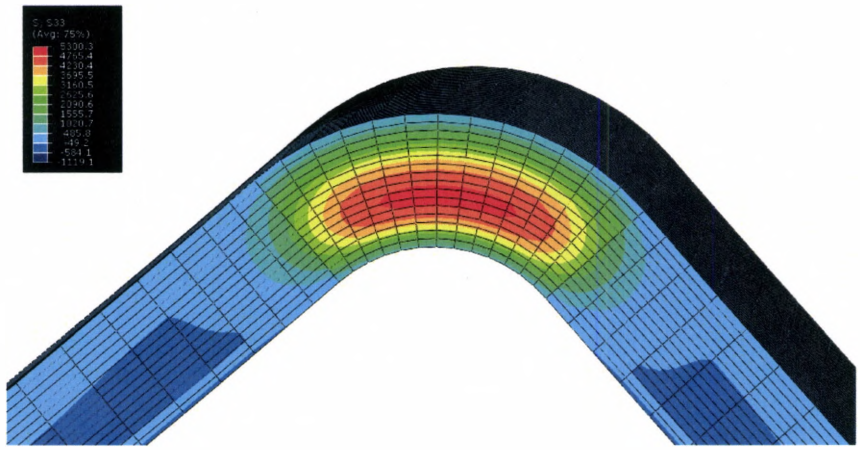

Figure 29. ABAQUS Results of Through-the-Thickness Stress for 0.25"-Radius 16-Ply Bracket Without NMR at 321.7 lb Load

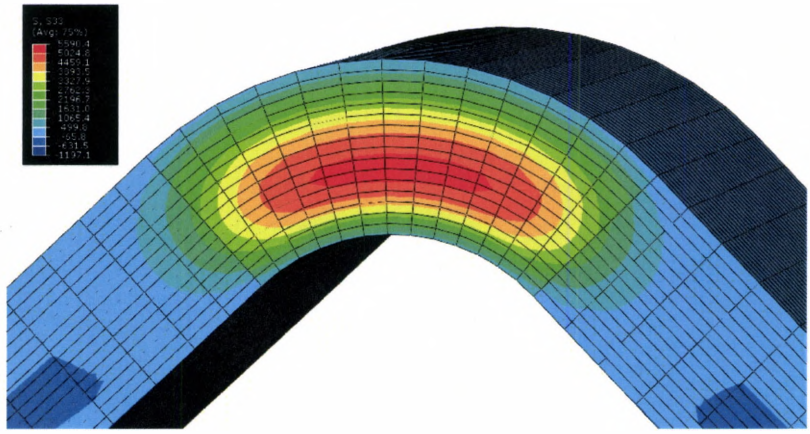

Figure 30. ABAQUS Results of Through-the-Thickness Stress for 0.25"-Radius 16-Ply Bracket Without NMR at 340.8 lb Load

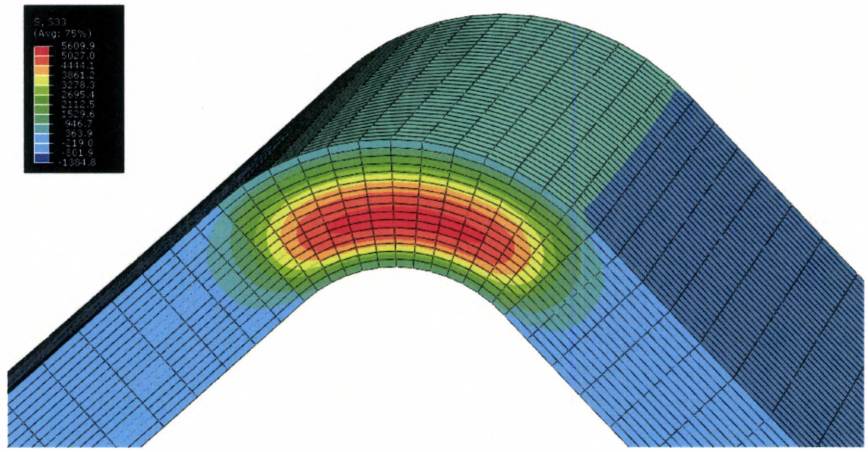

Figure 31. ABAQUS Results of Through-the-Thickness Stress for 0.25"-Radius 16-Ply Bracket With NMR at 394.3 lb Load

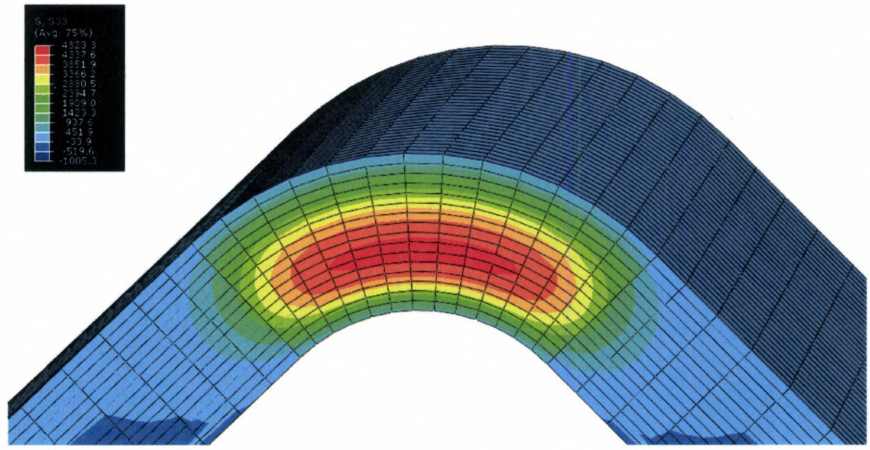

Figure 32. ABAQUS Results of Through-the-Thickness Stress for 0.25"-Radius 16-Ply Bracket With NMR at 291.5 lb Load

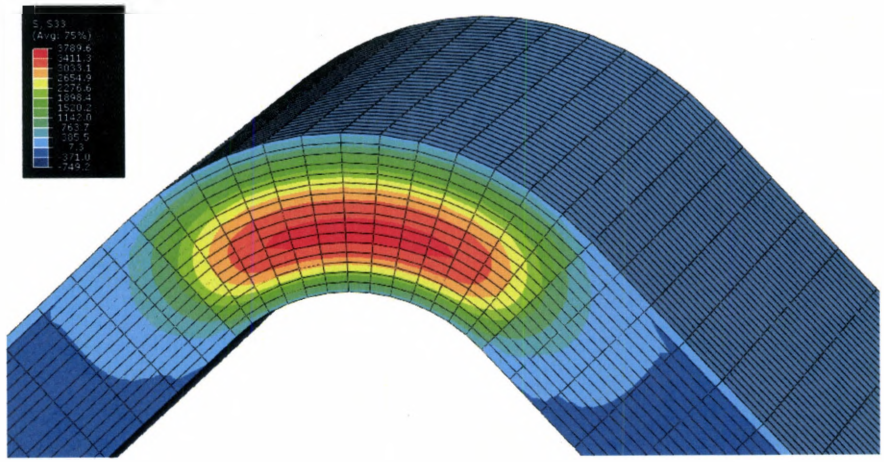

Figure 33. ABAQUS Results of Through-the-Thickness Stress for 0.25"-Radius 16-Ply Bracket With NMR at 225.5 lb Load

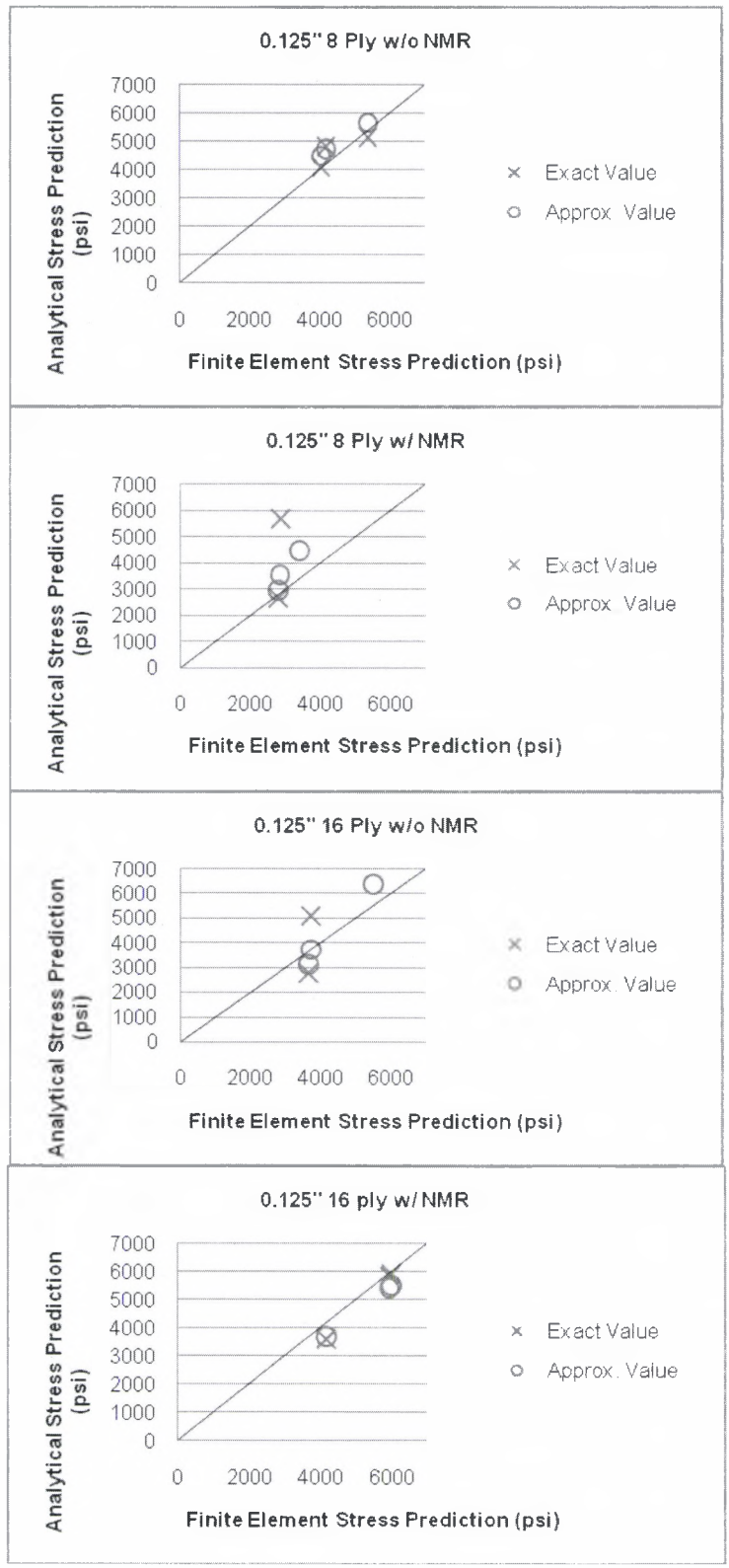

Figure 34. Comparison of Analytical Stress Prediction and Finite Element Stress Prediction of 0.125"-Radius Specimens

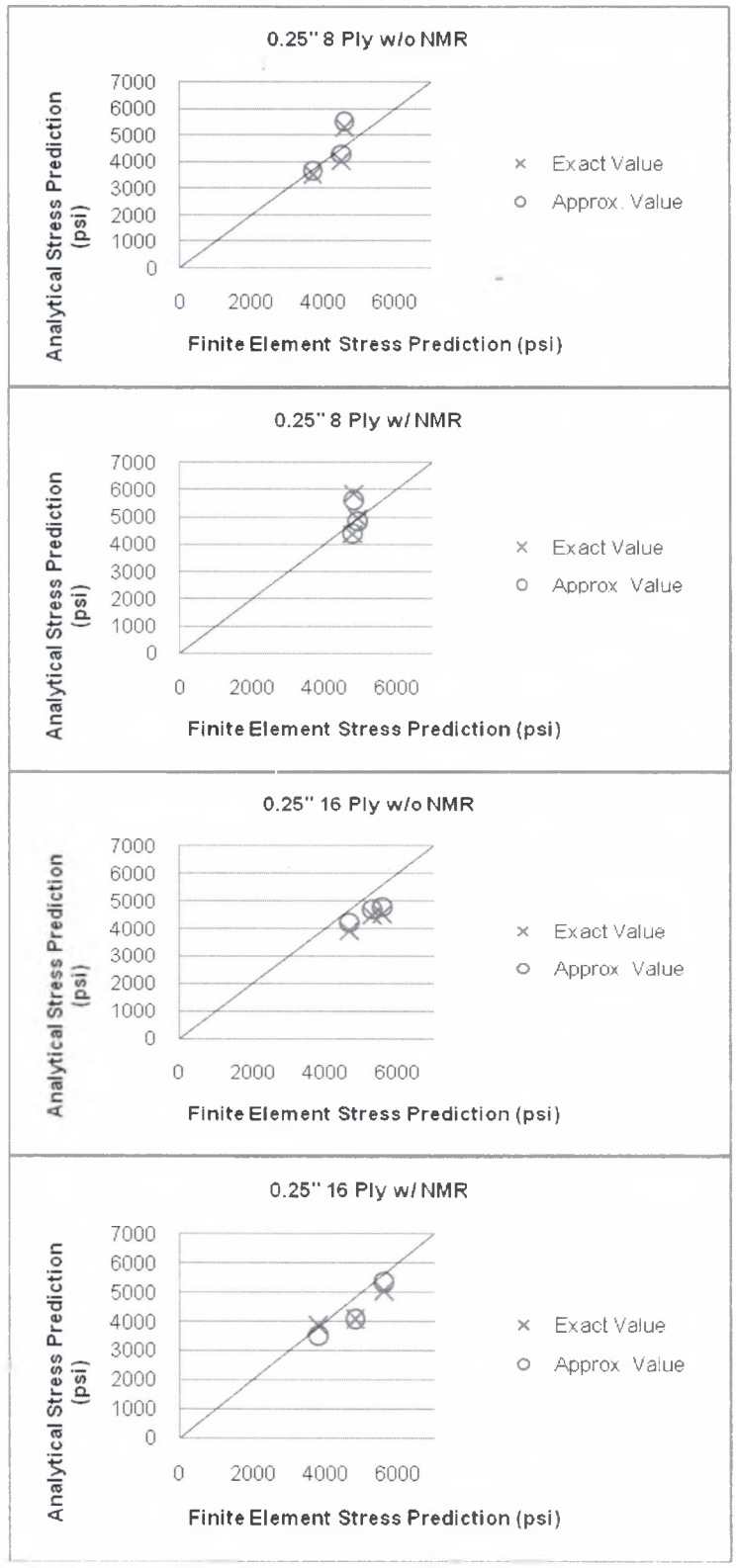

Figure 35. Comparison of Analytical Stress Prediction and Finite Element Stress Prediction of 0.25"-Radius Specimens

exact and approximate equations and the finite element analysis correlate reasonably well with one another.

The critical radial stress result appeared to be independent of the beam radius, thickness, and nano-scale additive. This can be seen from looking at Figure 36 which compares the variables to the maximum radial stress. The NMR specimens, however, showed a somewhat greater level of variability in the critical values of maximum radial stress (Table 4). There is a minor decrease in critical radial stress values for the 8-ply 0.125-inch specimens with NMR and a minor increase for the 16-ply 0.125-inch specimens with NMR. The stress values for all 0.25-inch brackets with and without NMR remain around the same value. Graphs showing the overall effects of NMR for each specimen type can be seen in Figure 37. It was found that, despite a three-fold difference in failure load and curved beam strength, the critical value of radial out-of-plane interlaminar peel stress (radial peel stress at initial failure) ranged between 4,300 to 4,700 psi. This is comparable to 6,900 psi, which was the resulting interlaminar peel stress calculated in reference 9 for a 16-ply graphite/epoxy composite with a higher modulus, E1.

Two different types of behavior were demonstrated during the failure of the angle brackets as seen in Figures 38 - 45. An example of the first type of behavior can be seen in Figure 38. The graph shows the force versus displacement of a specimen that reached a 50 percent decrease in load on the first drop. The second type of behavior can be seen in Figure 39. The graph shows the force versus displacement of one of the specimens that retained load

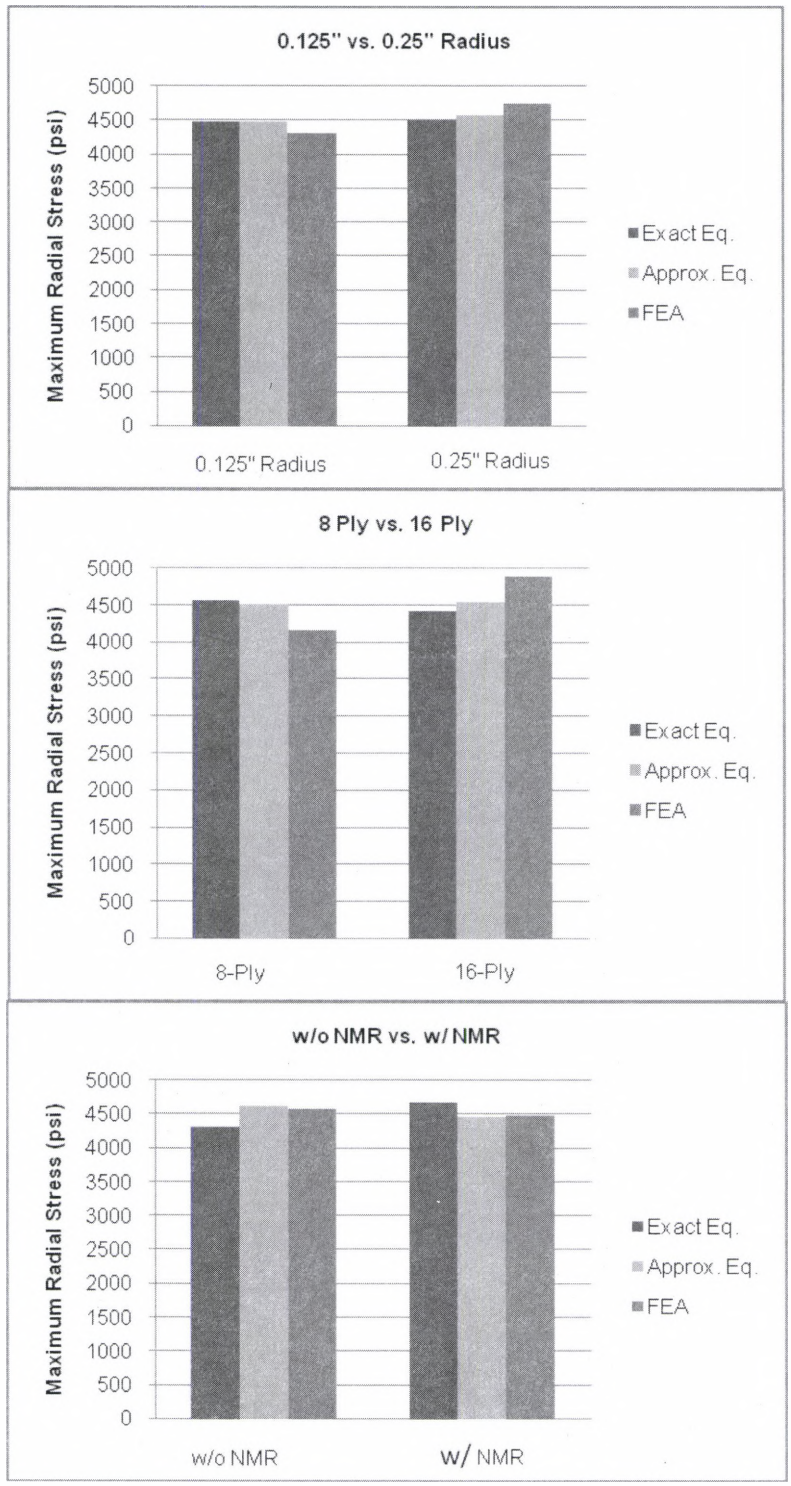

Figure 36. Variable Study for Maximum Radial Stress at Failure Initiation

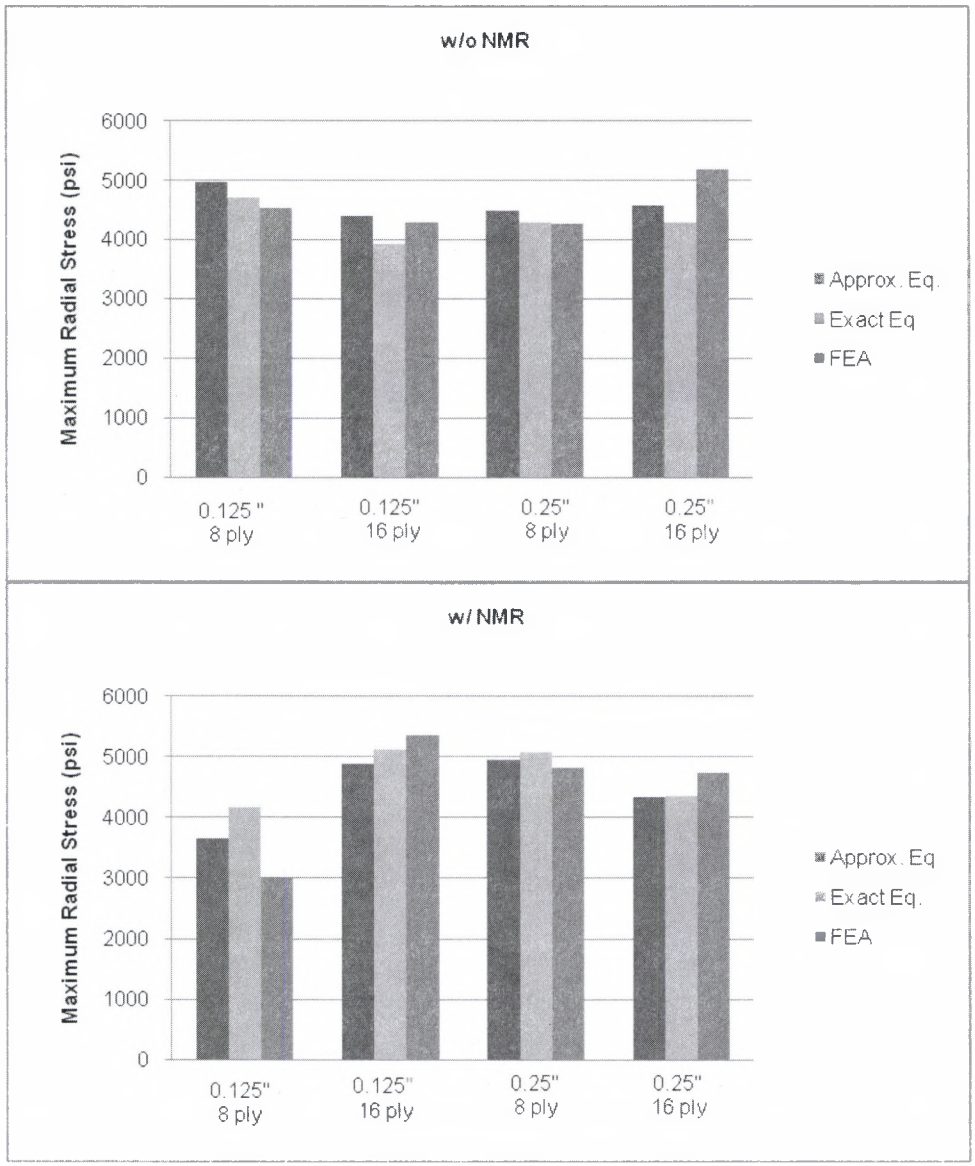

Figure 37. Nano-Material Comparison

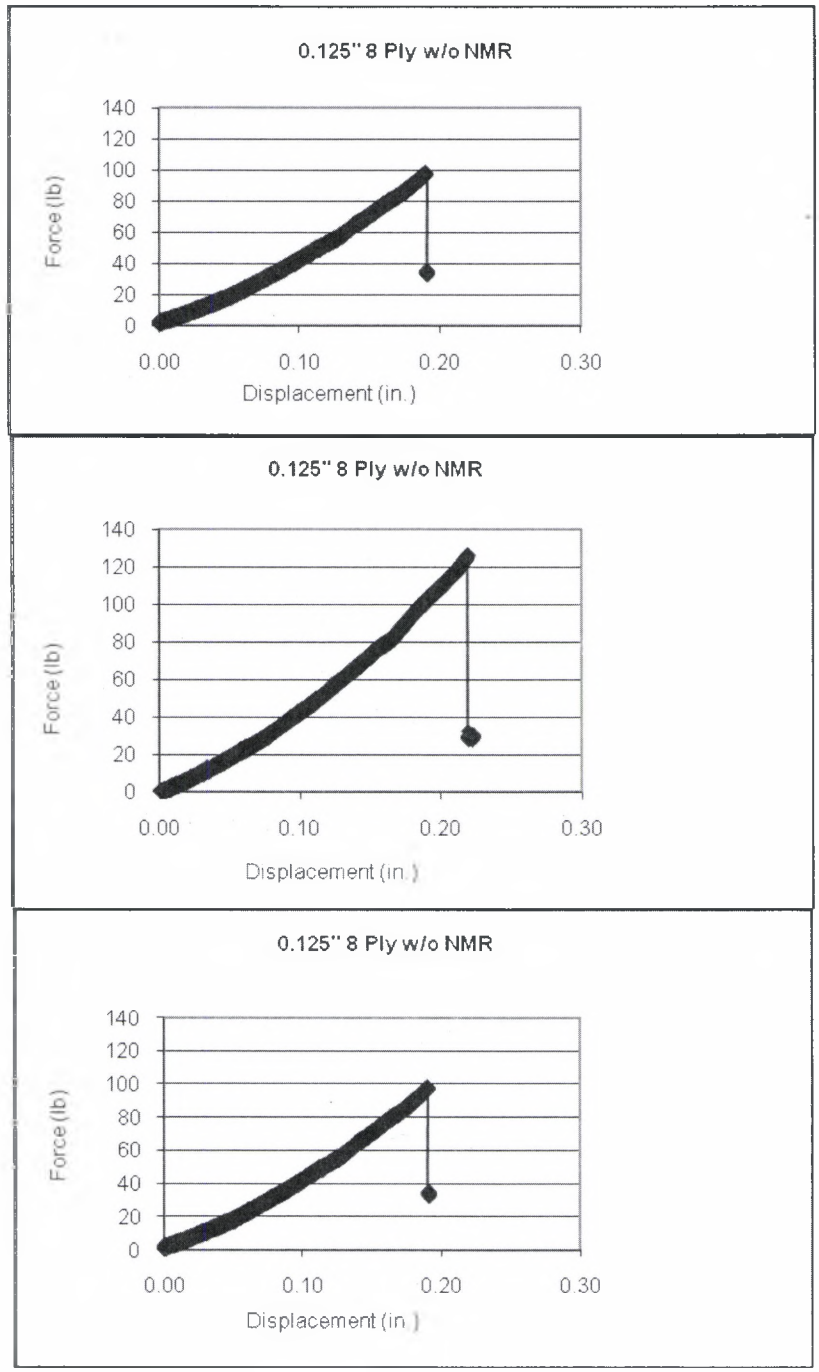

Figure 38. Force versus Displacement for 0.125"-Radius 8-Ply Specimens Without NMR

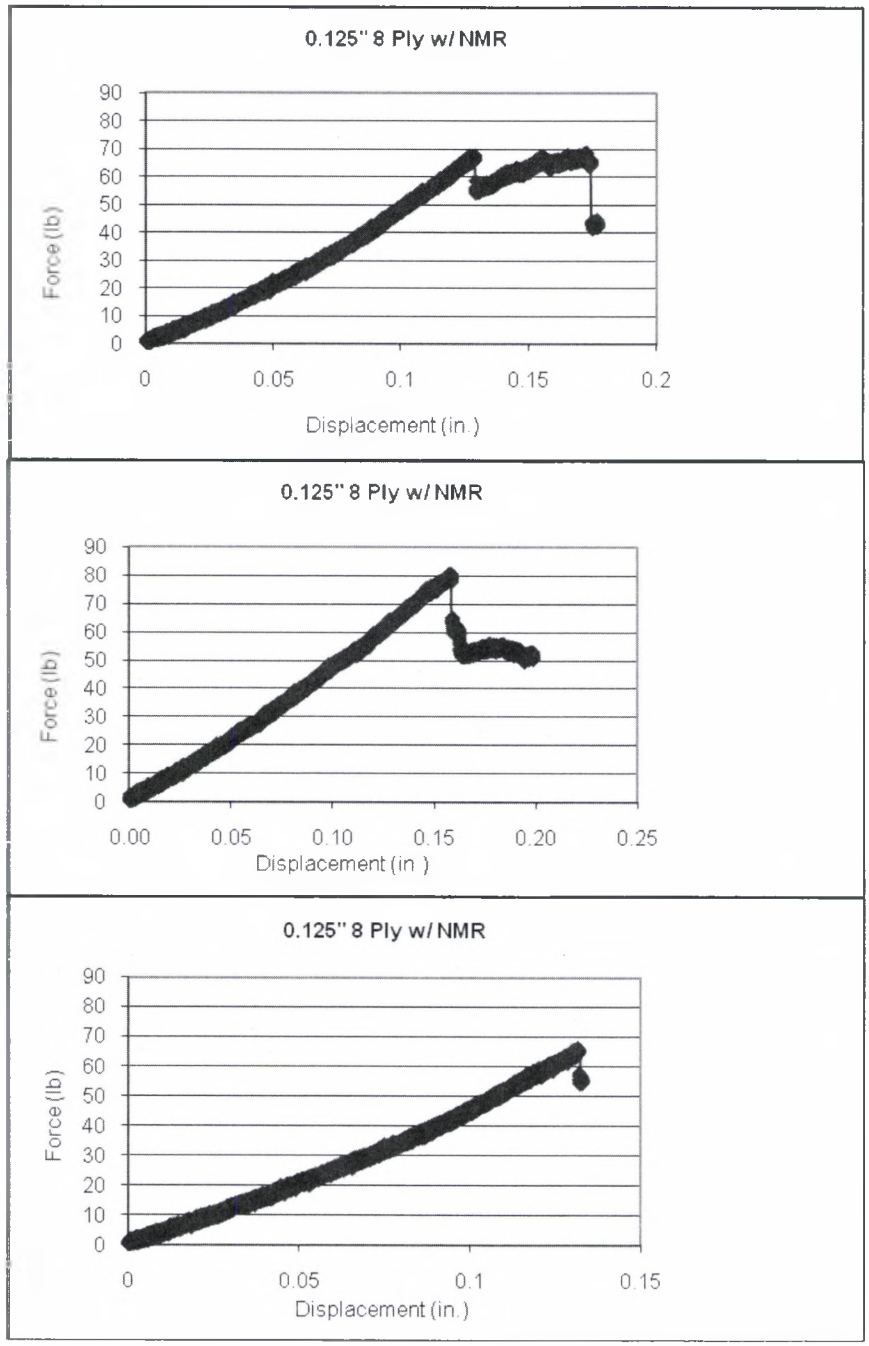

Figure 39. Force Versus Displacement for 0.125"-Radius 8-Ply Specimens With NMR

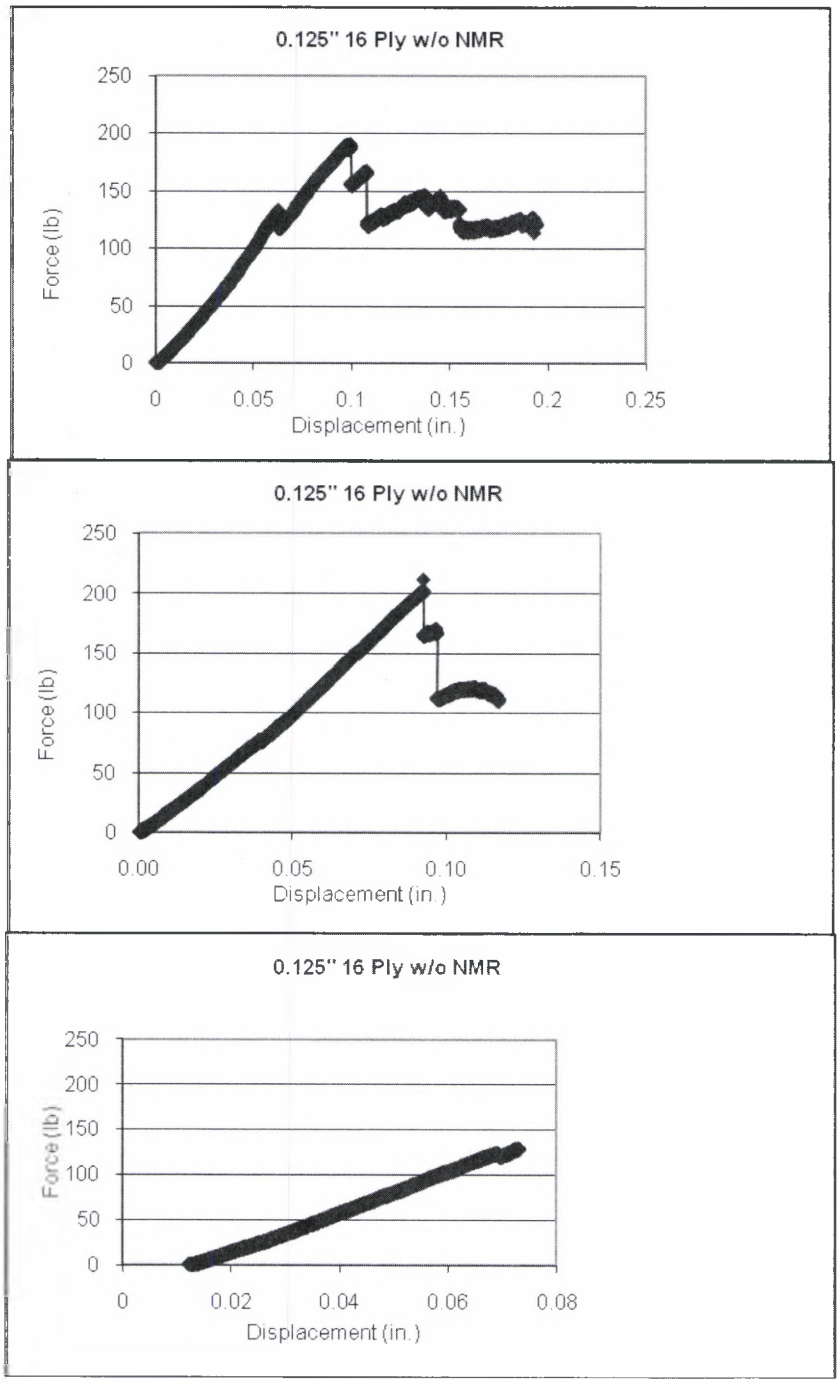

Figure 40. Force Versus Displacement for 0.125"-Radius 16-Ply Specimens Without NMR

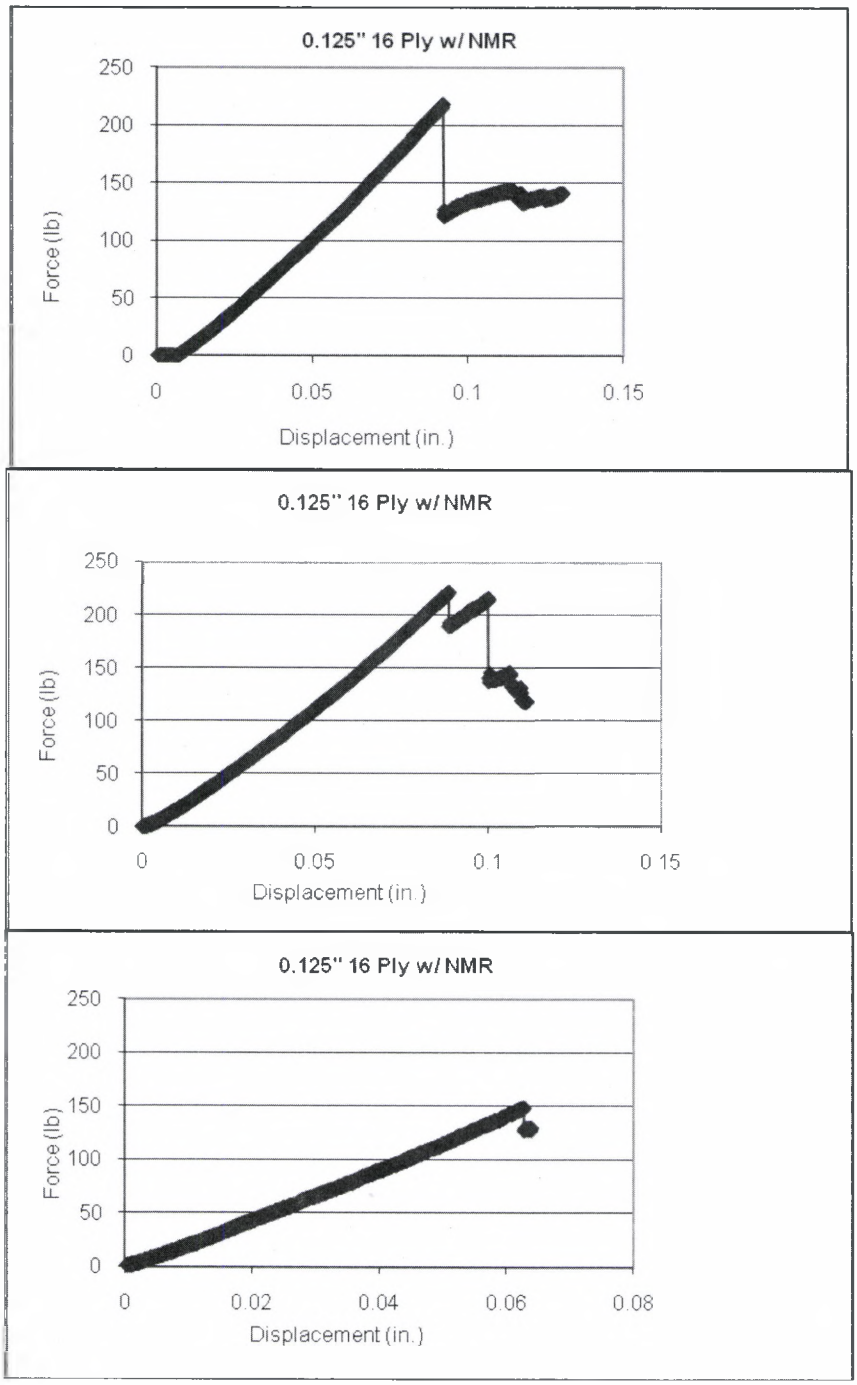

Figure 41. Force Versus Displacement for 0.125"-Radius 16-Ply Specimens With NMR

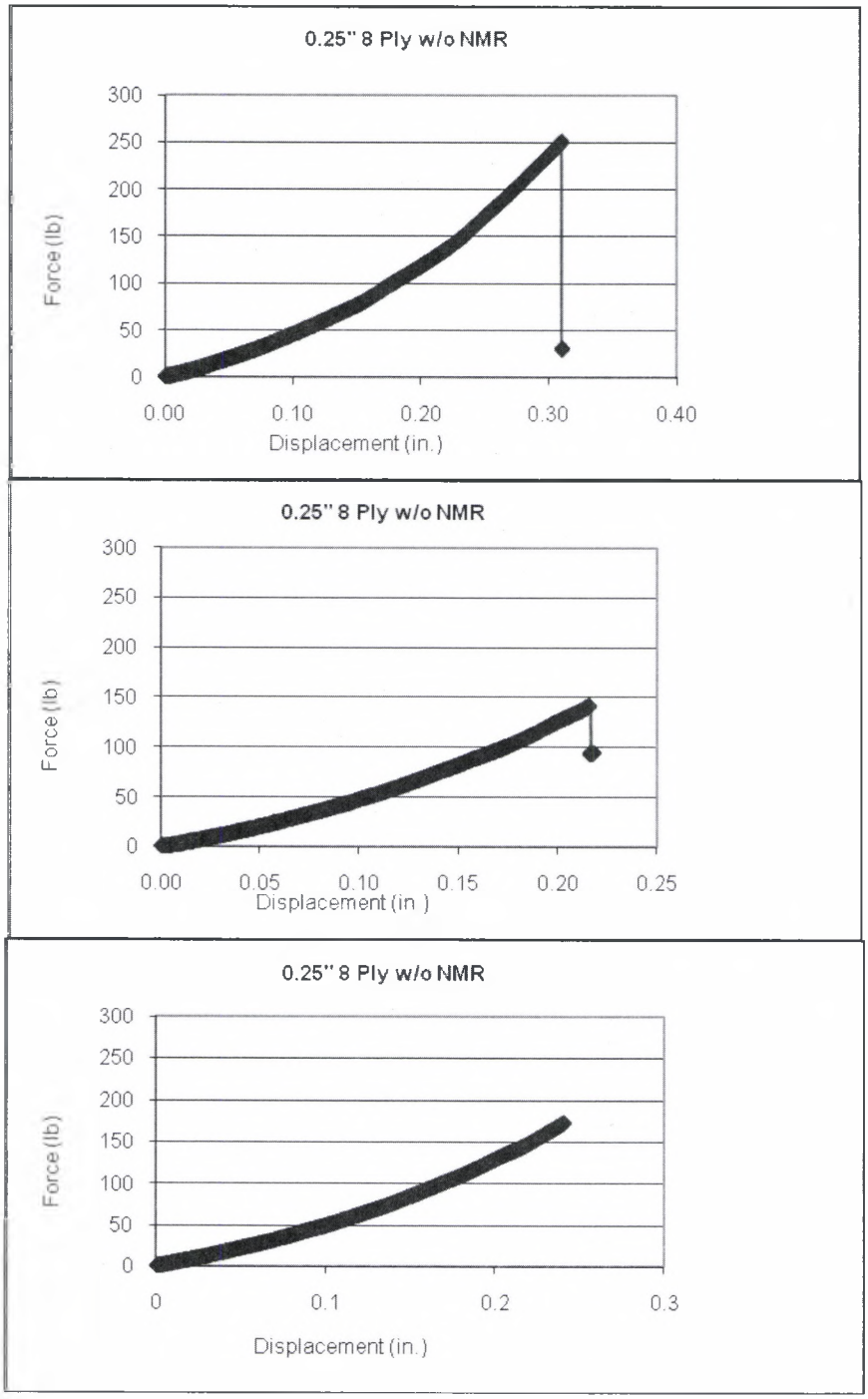

Figure 42. Force Versus Displacement for 0.25"-Radius 8-Ply Specimens Without NMR

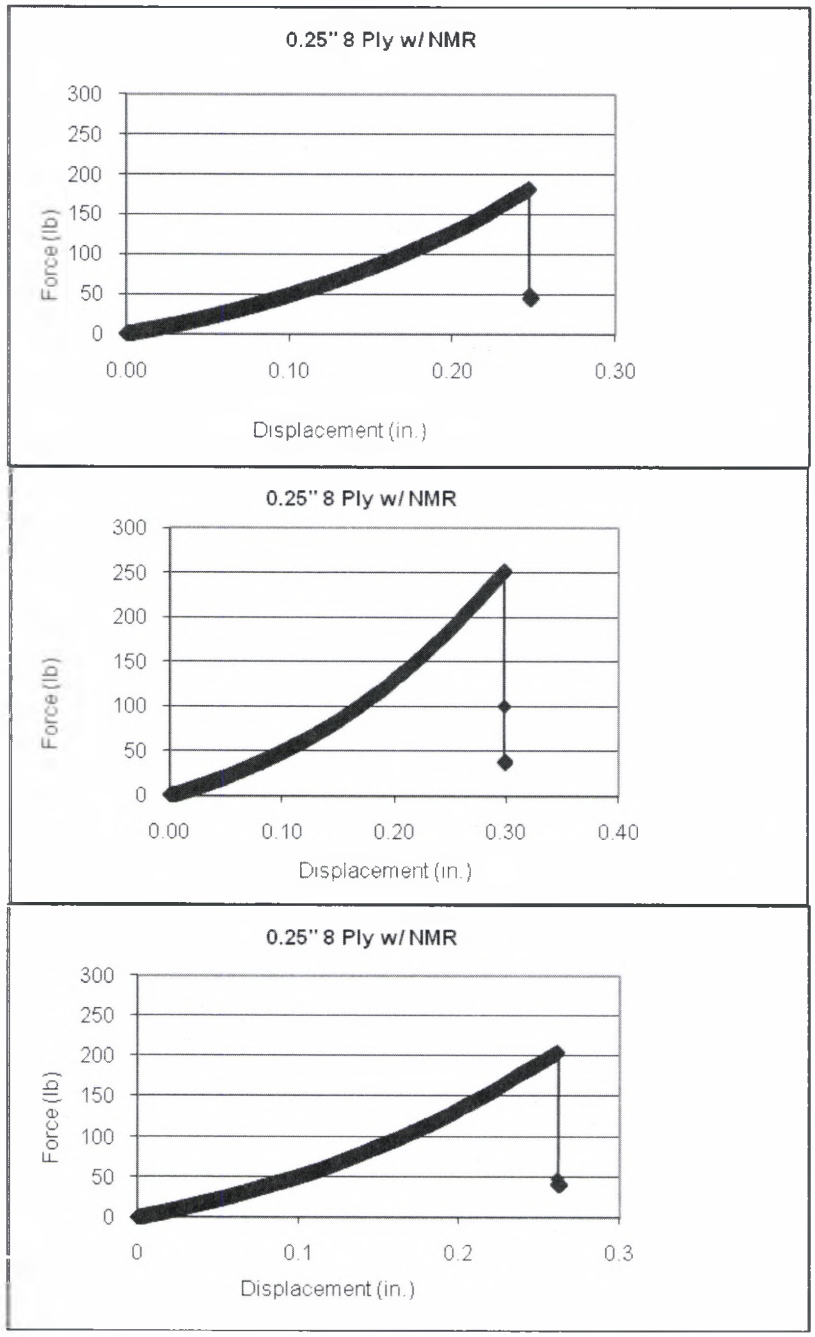

Figure 43. Force Versus Displacement for 0.25"-Radius 8-Ply Specimens With NMR

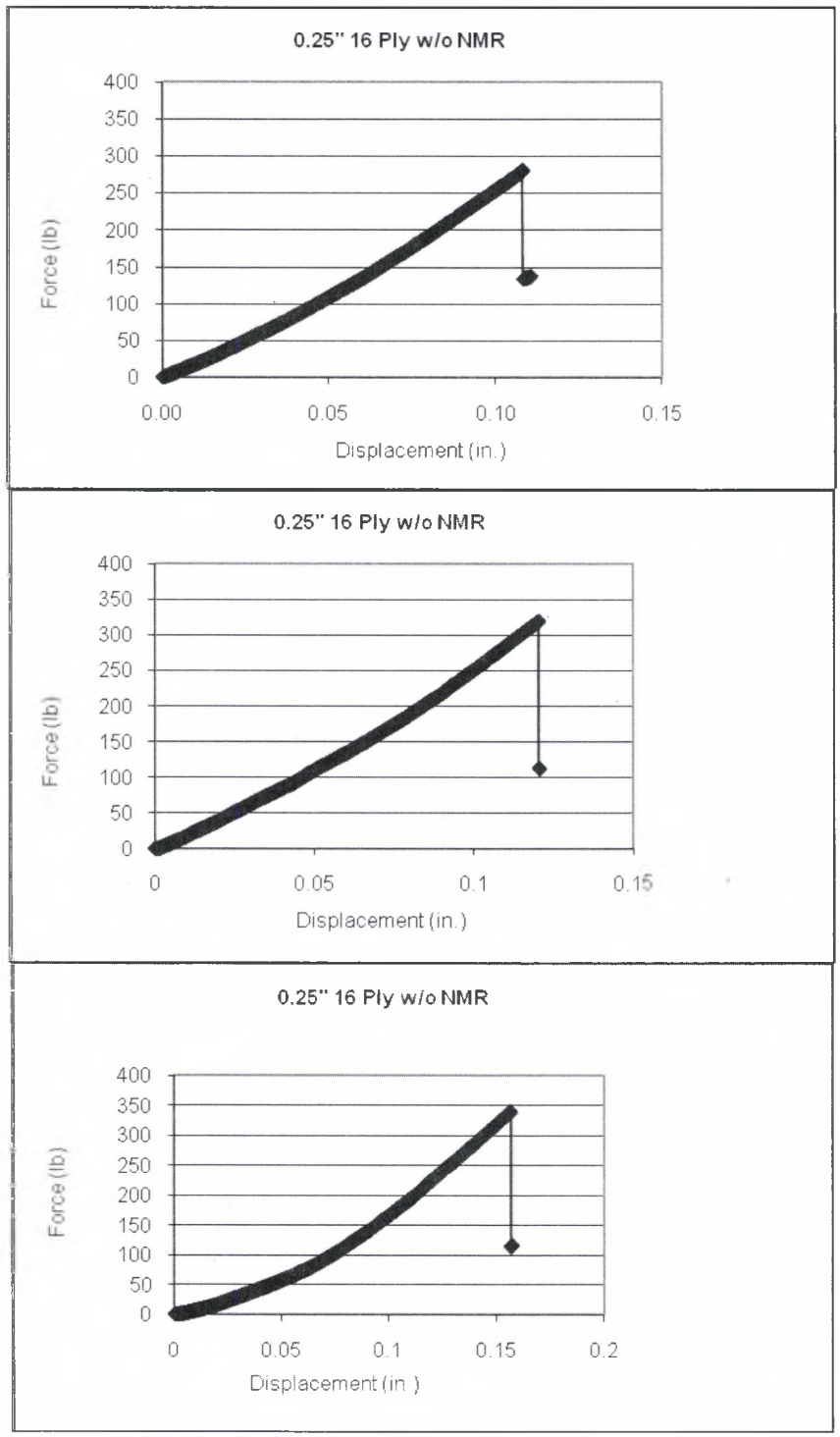

Figure 44. Force Versus Displacement for 0.25"-Radius 16-Ply Specimens Without NMR

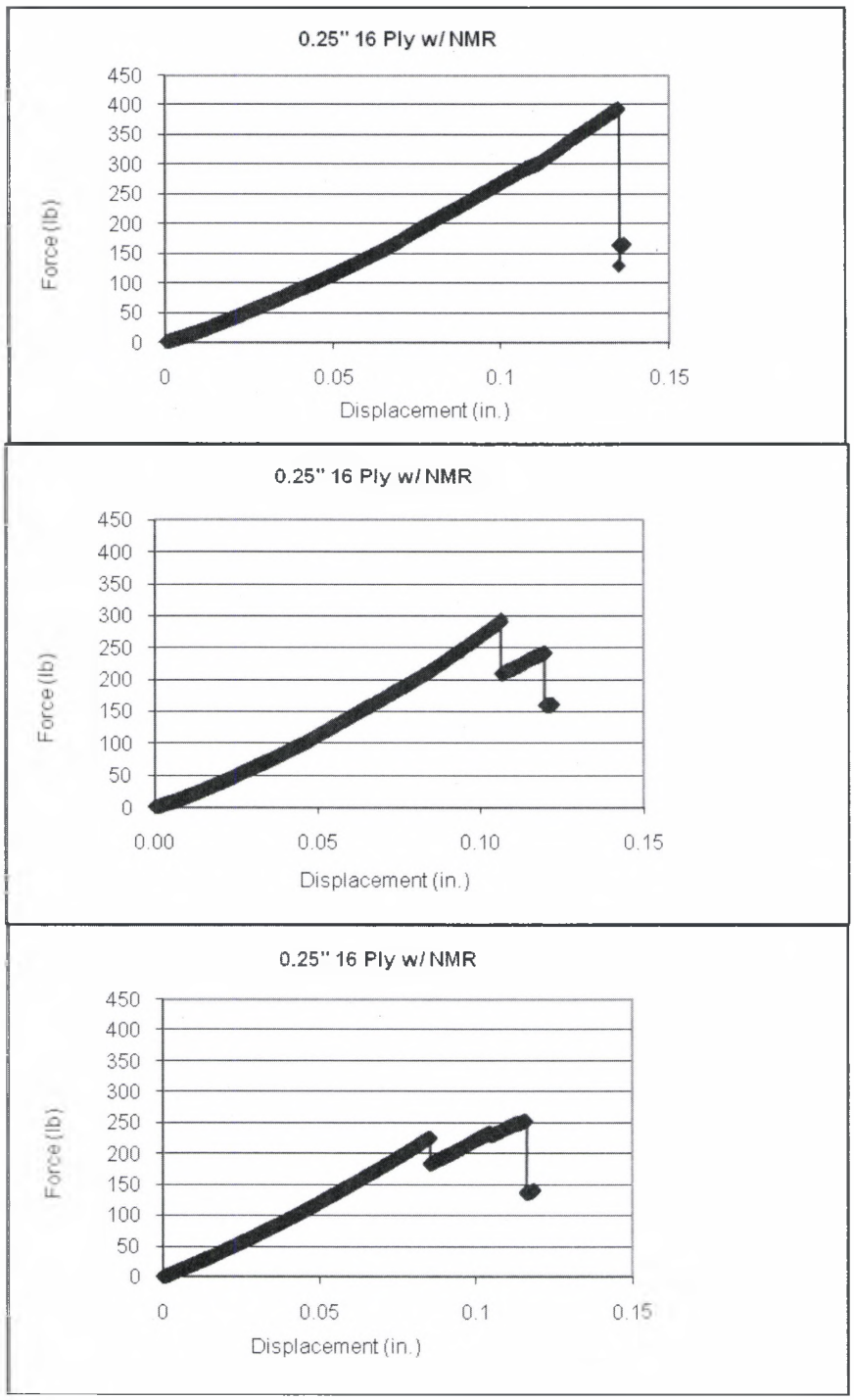

Figure 45. Force Versus Displacement for 0.25"-Radius 16-Ply Specimens With NMR

for a period of time after initial failure but before it reached a 50 percent of the peak load (stick-slip behavior). When only comparing the 0.125-inch and 0.25-inch radius specimens, it was determined that the majority of the 0.125-inch radius brackets experienced the stick-slip behavior. When analyzing the thickness, the majority of the 16-ply brackets experienced the stick-slip behavior and the 8-ply, the sharp load drop. Addition of the nano-scale additive tended to alter the failure mode from a rapid load drop in the non-NMR cases, to stick-slip type of loading in the specimens with the NMR, hence increasing damage tolerance and energy absorption.

Micrograph pictures were taken for each specimen type tested. The specimens were tested using the four-point bend test until their first load drop. They were then removed from the MTS load frame to ensure that the initial failure could be examined. Micrographs for the eight different types of specimens tested can be seen in Figures 46 – 61. When looking at the photomicrographs, it can be concluded that two different types of failure exist: brackets that failed with a single crack, and brackets that failed with multiple cracks. For example, see Figure 49 with a single crack and Figure 55 with multiple cracks. The majority of the 0.125-inch radius brackets failed with a single crack, while all of the 0.25-inch radius brackets had multiple cracks. It was also noted that the specimens that experienced a 50 percent drop from their peak load, were most likely to fail with multiple cracks. Table 5 presents a comparison of the failure mode (single or multiple cracks) and the failure behavior (stick-slip or drop) between the different variables.

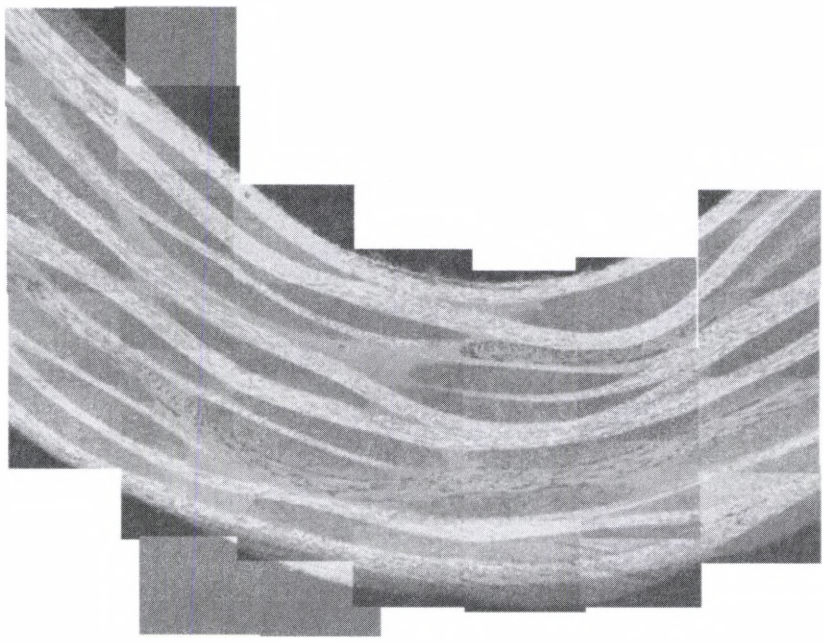

Figure 46. Photomicrograph of 0.125"-Radius 8-Ply Bracket Without NMR Before Applied Load

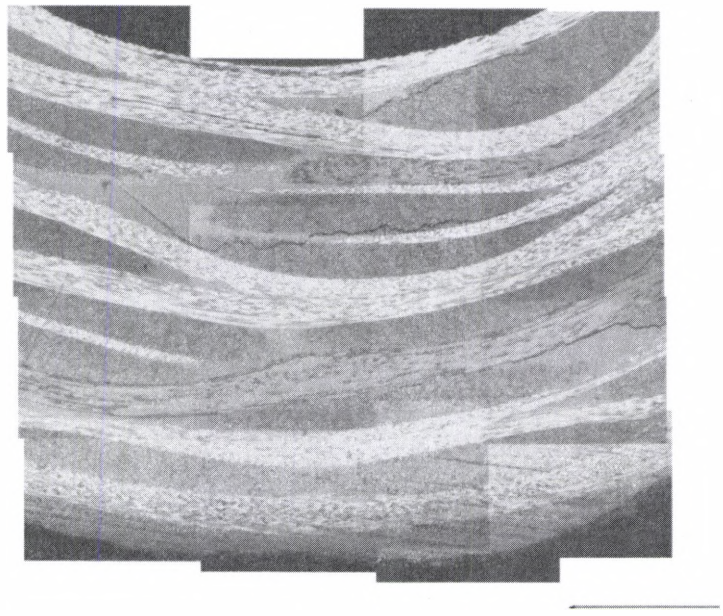

Figure 47. Photomicrograph of 0.125"-Radius 8-Ply Bracket Without NMR After Applied Load

Figure 48. Photomicrograph of 0.125"-Radius 8-Ply Bracket With NMR Before Applied Load

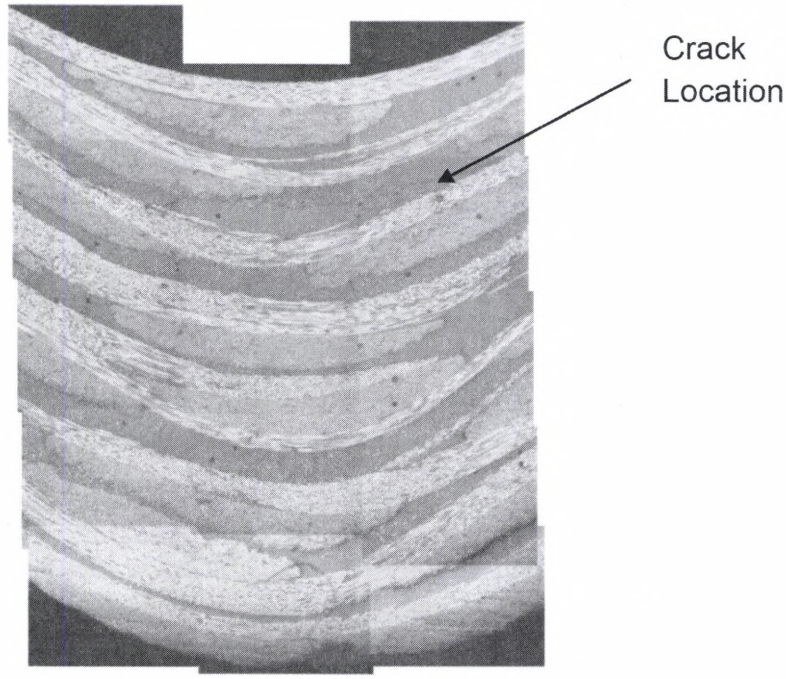

Figure 49. Photomicrograph of 0.125"-Radius 8-Ply Bracket With NMR After Applied Load

Figure 50. Photomicrograph of 0.125"-Radius 16-Ply Bracket Without NMR Before Applied Load

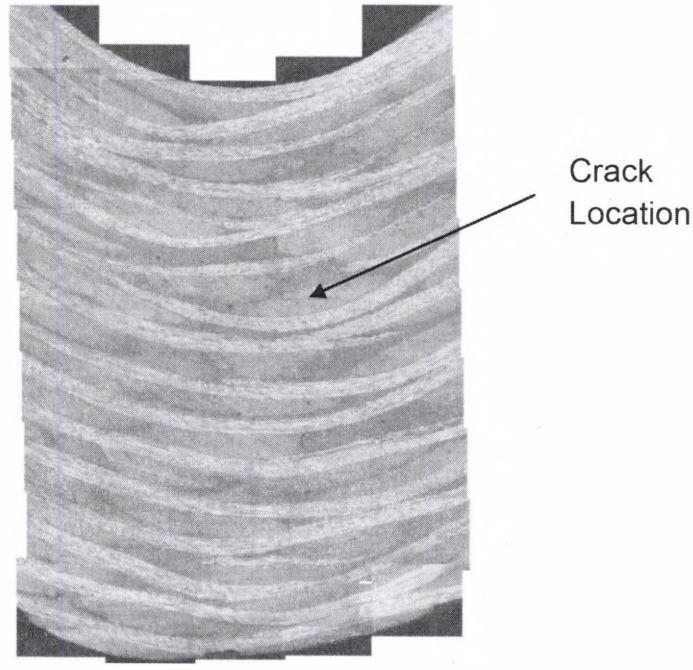

Figure 51. Photomicrograph of 0.125"-Radius 16-Ply Bracket Without NMR After Applied Load

Figure 52. Photomicrograph of 0.125"-Radius 16-Ply Bracket With NMR Before Applied Load

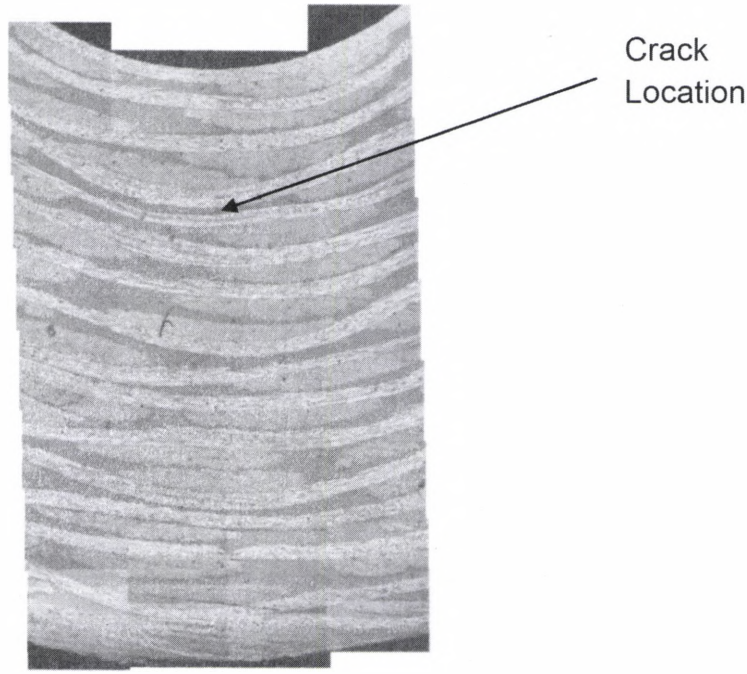

Figure 53. Photomicrograph of 0.125"-Radius 16-Ply Bracket With NMR After Applied Load

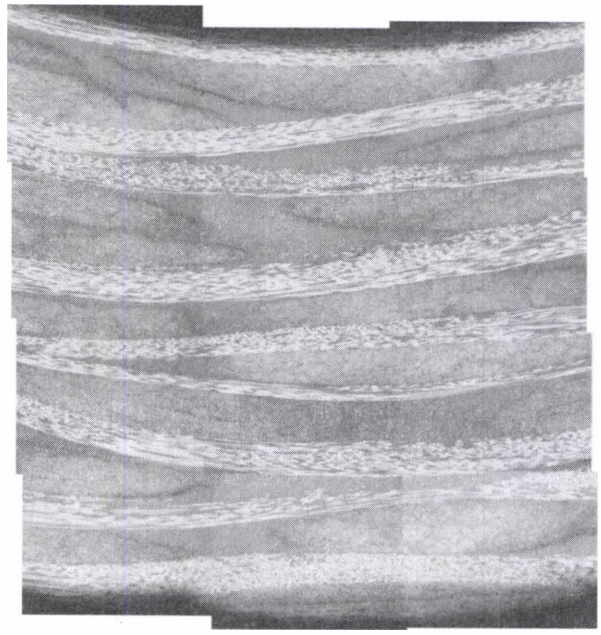

Figure 54. Photomicrograph of 0.25"-Radius 8-Ply Bracket Without NMR Before Applied Load

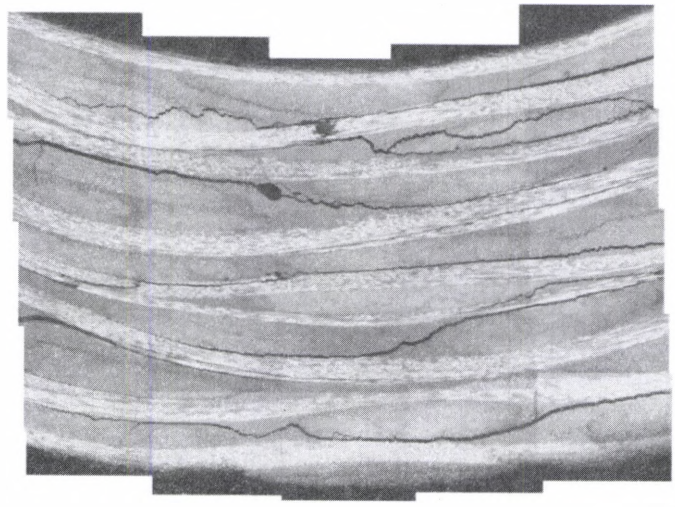

Figure 55. Photomicrograph of 0.25"-Radius 8-Ply Bracket Without NMR After Applied Load

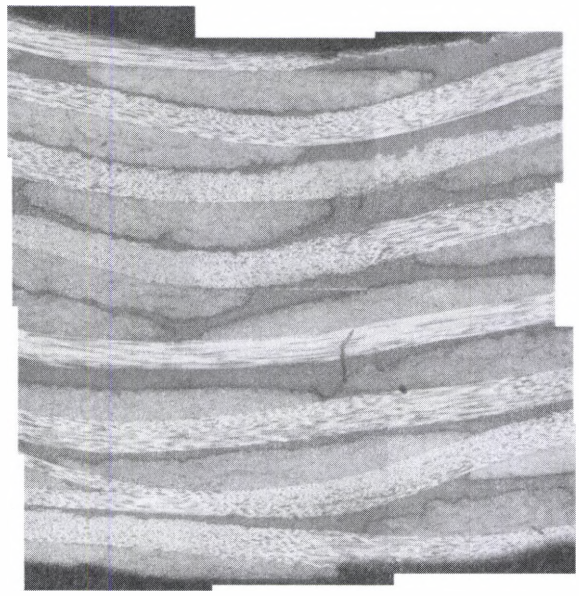

Figure 56. Photomicrograph of 0.25"-Radius 8-Ply Bracket With NMR Before Applied Load

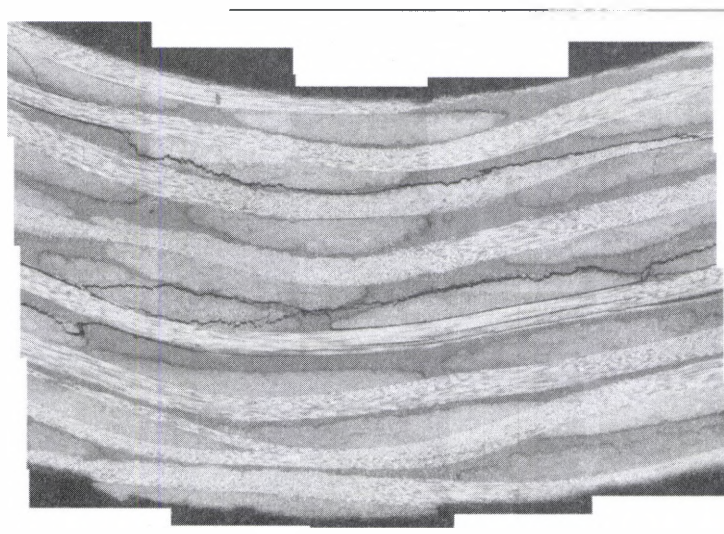

Figure 57. Photomicrograph of 0.25"-Radius 8-Ply Bracket With NMR After Applied Load

Figure 58. Photomicrograph of 0.25"-Radius 16-Ply Bracket Without NMR Before Applied Load

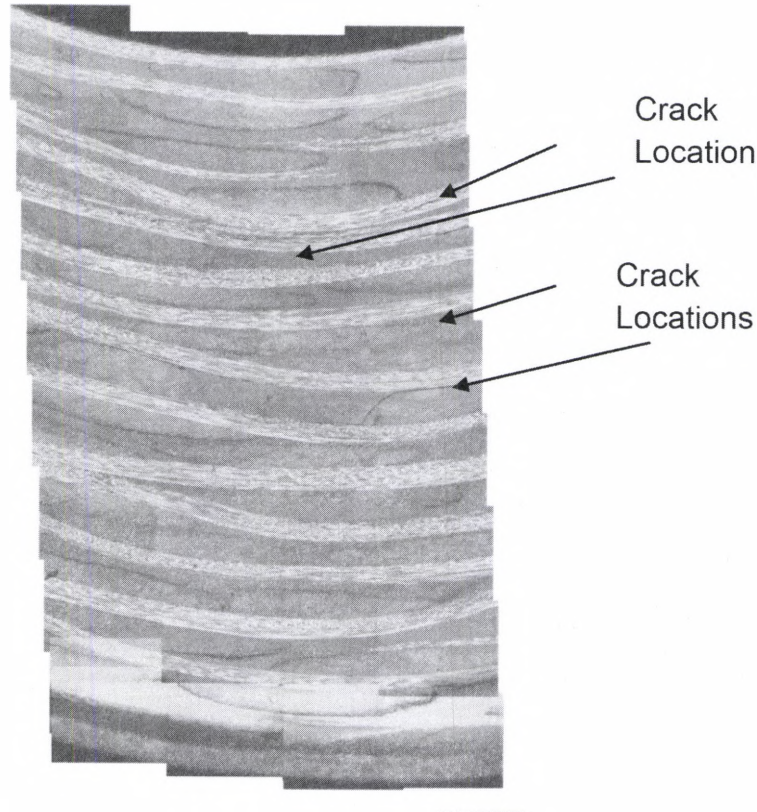

Figure 59. Photomicrograph of 0.25"-Radius 16-Ply Bracket Without NMR After Applied Load

Figure 60. Photomicrograph of 0.25”-Radius 16-Ply Bracket With NMR Before Applied Load

Figure 61. Photomicrograph of 0.25”-Radius 16-Ply Bracket With NMR After Applied Load

TABLE 5. FAILURE MODE AND BEHAVIOR		
Factors	Failure Mode	Failure Behavior
0.125" Radius	3/4 Single Cracks	9/12 Stick-Slip
0.25" Radius	4/4 Multiple Cracks	10/12 Stick-Slip
8 ply	3/4 Multiple Cracks	9/12 Rapid Load Drop
16 ply	1/2 Multiple Cracks; 1/2 Single Cracks	9/12 Stick-Slip
w/o NMR	3/4 Multiple Cracks	9/12 Rapid Load Drop
w/ NMR	1/2 Multiple Cracks; 1/2 Single Cracks	9/12 Stick-Slip

When analyzing the photomicrographs and the results from ABAQUS, it can also be concluded that the location of the crack paths and location of the maximum through-the-thickness stress correlate well with one another. For example, when looking at Figure 22, the ABAQUS results for the 0.125-inch radius 16-ply specimen without NMR, and Figure 51, the corresponding photomicrograph, it can be concluded that the maximum radial stress location in ABAQUS and the crack path in the photomicrograph are both within the vicinity of the fourth through eighth ply (from the inside of the bend). The same applies for the other bracket specimens.

Finally, the location of the crack path was examined in order to see if a relationship could be made between the failure and the location of the nanofibers. When comparing the photomicrographs of the composites with nanofiber and without nanofiber, no distinction was able to be made between the two. The actual nanofibers were not able to be seen in the photomicrographs. Since the nanofiber location was not able to be determined through the use of photomicrographs, the assumption that the nanofibers were located between the plies was used. As previously stated, the curing process should cause the

majority of the nanofibers to remain between the plies [23, 24]. Typically, when there is a thicker region of resin between the plies, there are more nanofibers present [23, 24]. The addition of nanofiber could be the reason behind the better distinction of plies for composites with NMR. When looking at the crack paths in each of the photomicrographs, it was seen that multiple types of failure paths exist: composites failed with cracks located on the interfaces between the resin and fiber, cracks only within the fiber, and cracks only within the resin. A valid conclusion was not able to be made about the location of the nanofibers and the failure path. The complexity of the failure modes at the microscale (for example, crack paths in the vicinity of fiber tows, resin rich zones, etc.) make clear that the critical radial stress values calculated, while of high engineering value, do not account for the detailed microstructural effects.

The effect of curvature was also taken into account in Table 6. The ratios of the thicknesses and inner radii were calculated for each of the different types of brackets, and compared to their failure behavior. Table 6 was divided in two categories: without NMR and with NMR. A distinct pattern exists for each category. When comparing the brackets located in the column without NMR, it was found that the specimen with the highest ratio was the only bracket to experience the stick-slip behavior. This specific angle bracket had a 0.125 inch radius with 16 plies. When looking at the specimens in the NMR category, it was determined that the bracket with the lowest ratio was the only specimen to experience an instant 50 percent load drop. Brackets constructed with higher ratios have more of a tendency to have the stick-slip behavior, while brackets

TABLE 6. CURVATURE EFFECT			
Variables	t/r_i	w/o NMR	w/ NMR
0.125" 8 ply	0.896	Drop	Stick-Slip
0.125" 16 ply	1.792	Stick-Slip	Stick-Slip
0.25" 8 ply	0.448	Drop	Drop
0.25" 16 ply	0.896	Drop	Stick-Slip

with lower ratios tend to have a sharp load drop. The brackets with the nano-materials are inclined to encompass the stick-slip behavior, while the brackets without, are more likely to undergo a sharp load drop.

Finally, a comparison was made between the approximate maximum radial stress equations used in ASTM D6415 equations and the approximate maximum radial stress equations presented in Reference [3]. It should be noted that the Kedward, Wilson, and McLean text presents three approximate equations for radial stress, one of them being the same equation that was used in the ASTM D6415 standard (Eq. 9). All three equations (Eq. 9-11) are plotted together for the different specimens in Figures 62 and 63. The equations agree reasonably well for all of the specimens tested, except for the second specimen for the 0.125 inch radius 8 ply with NMR and the second specimen for the 0 .125 inch radius 16 ply without NMR. This disagreement is due to the fabrication defects around the radius of these specimens, as previously stated. Both specimens had a variation in the thickness around the radius.

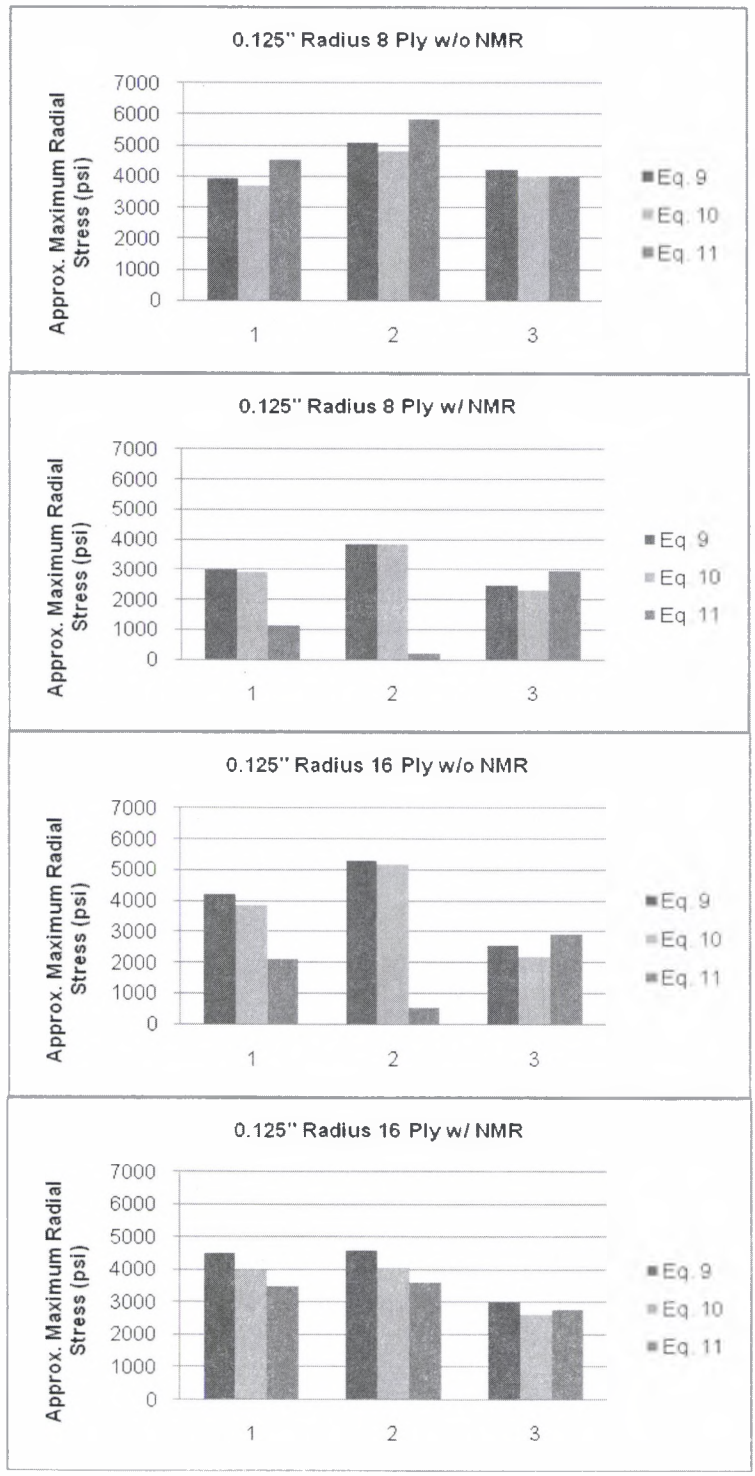

Figure 62. Approximate Maximum Radial Stress for 0.125"-Radius Specimens with 8- and 16-Plies With and Without NMR

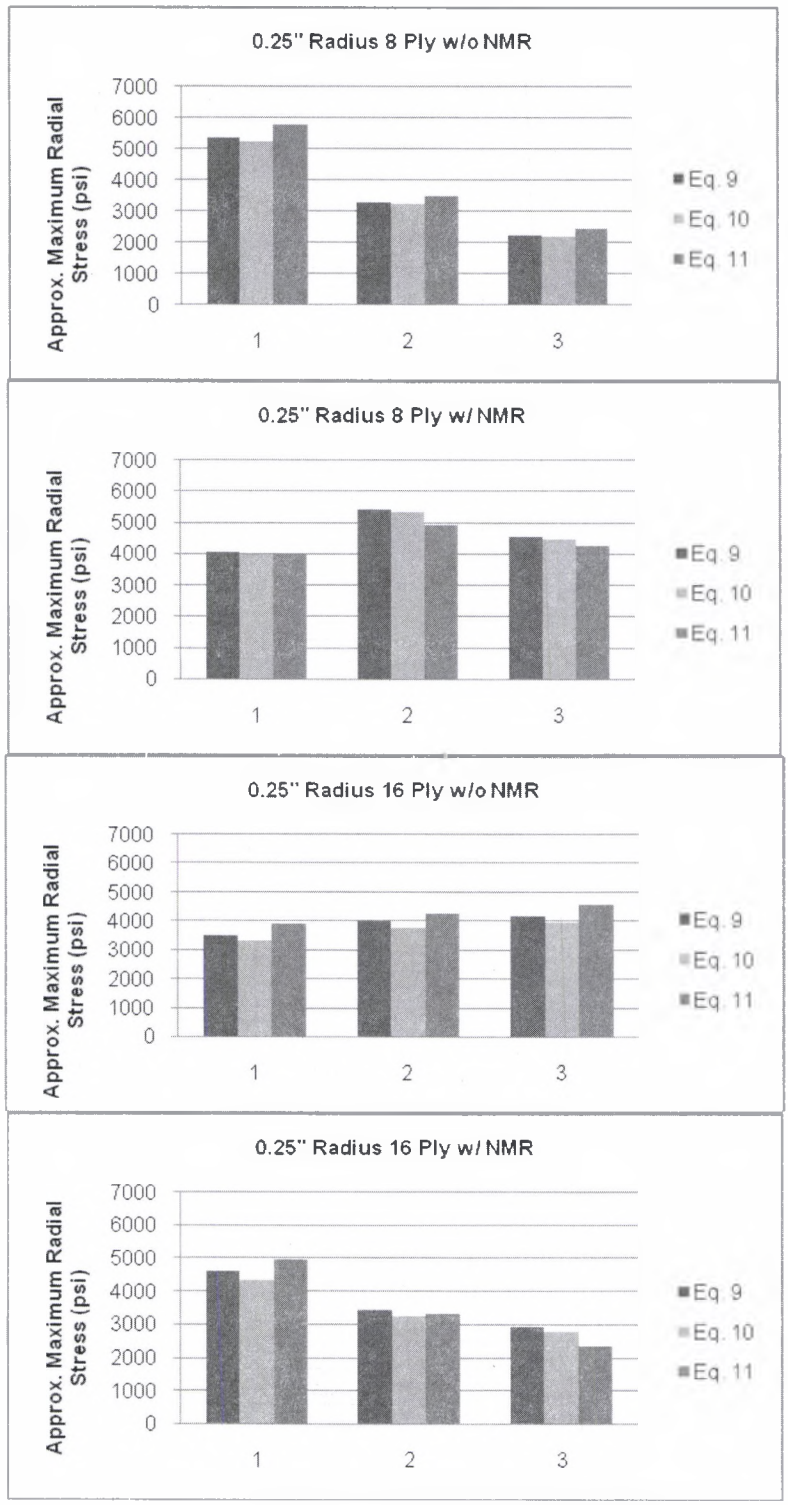

Figure 63. Approximate Maximum Radial Stress for 0.25"-Radius Specimens with 8- and 16-Plies With and Without NMR

CHAPTER VIII

CONCLUSIONS

The behavior of composite brackets (beams with sharp 90° bends) was investigated. In particular, the bend radius, laminate thickness, and addition of nano-scale vapor grown carbon fiber (ASI PR-24-XT-OX added to the resin) were considered as study variables. The specimens were fabricated from carbon fiber (AS4) 5 harness satin cloth reinforcing Epon 862 epoxy (both with and without the carbon nano fiber). The specimens were subjected to four-point bending according to ASTM D6415. Closed form and 3D finite element solutions were used to reduce the data. It was found that, despite a three-fold difference in failure load and curved beam strength, the critical value of radial out-of-plane interlaminar peel stress (radial peel stress at initial failure) ranged between 4,300 – 4,700 psi. The critical radial stress result appeared to be independent of the beam radius, thickness, and nano-scale additive. The NMR specimens, however, showed a greater level of variability in the critical values of maximum radial stress. Addition of the nano-scale additive tended to alter the failure mode from a rapid load drop in the non-NMR resin cases, to stick-slip type of loading in the specimens with the nano-scale reinforcement, hence increasing damage tolerance and energy absorption. The majority of the specimens without NMR

experienced a catastrophic failure, with multiple cracks, while the majority of the specimens with NMR failed with only a single crack. The location of the failure was found to occur in the vicinity of the maximum through-the-thickness stress. Conclusions about the failure paths and locations of nanofiber were not able to be made due to the inconsistency of the failure paths.

Recommendations for future testing include investigation of the details of the nano-dispersion with respect to the fiber tows versus failure morphology and strength. In addition, the hot/wet and fatigue characteristics of NMR versus non-NMR reinforced resin should be investigated.

BIBLIOGRAPHY

1. Daniel, I. M. and O. Ishai. 2006. Engineering Mechanics of Composite Materials. 2nd ed. Oxford University Press, pp. 380.
2. ASTM D 6415/D 6415M – 06a, "Standard Test Method for Measuring the Curved Beam Strength of a Fiber-Reinforced Polymer-Matrix Composite," American Society of Testing Materials.
3. Kedward, K. T., R. S. Wilson, and S. K. McLean. 1989. "Flexure of Simply Curved Composite Shapes," Composites, 20(6): 527-536.
4. Layne, A. M. and L. A. Carlsson. 2002. "Test Method for Measuring Strength of a Curved Sandwich Beam," Experimental Mechanics, 42(2): 194-199.
5. Smidt, S. 1995. "Bending of curved sandwich beams," Composite Structures, 33: 211-225.
6. Smidt, S. 1996. "Bending of curved sandwich beams, a numerical approach," Composite Structures, 34: 279-290.
7. Ko, W. L. 1988. "Delamination Stresses in Semicircular Laminated Composite Bars," NASA, Technical Memorandum 4026.
8. Ko, W. L. and R. H. Jackson. 1989. "Multilayer Theory for Delamination Analysis of a Composite Curved Bar Subjected to End Forces and End Moments," NASA, Technical Memorandum 4139.

9. Shivakumar, K. N., H. G. Allen, and V.S. Avva. 1994. "Interlaminar Tension Strength of Graphite/Epoxy Composite Laminates," AIAA Journal, 32(7): 1478-1784.
10. Hiel, C. C., M. Sumich, and D. P. Chappell. 1990. "A Curved Beam Test Specimen for Determining the Interlaminar Tensile Strength of a Laminated Composite," Journal of Composite Materials, 25: 854-868.
11. Martin, R. H. 1992. "Delamination Failure in a Unidirectional Curved Composite Laminate," Composite Materials: Testing and Design), ASTM STP 1120, Glenn C. Grimes, Ed. American Society for Testing and Materials, 10: 365-383.
12. Sun, C. T. and S. R. Kelly. 1988. "Failure in Composite Angle Structures Part I: Initial Failure," Journal of Reinforced Plastics and Composites, 7: 220-232.
13. Martin, R. H. and W. C. Jackson.1993. "Damage Prediction in Cross-Plied Curved Composites Laminates," Composite Materials: Fatigue and Fracture, ASTM STP 1156, W. W. Stinchcomb and N. E. Ashbaugh, Eds., American Society for Testing and Materials, 4: 105-126.
14. Jackson, W. C. and R. H. Martin. 1993. "An Interlaminar Tensile Strength Specimen," Composite Materials: Testing and Design, ASTM STP 1206, E. T. Camponeschi, Jr., Ed., American Society for Testing and Materials, 11: 333-354.
15. Chang, F.-K. 1988. "The Strength Analysis of Wooden Bends," Environmental Effects on Composite Materials, pp.421-433.

16. Mason, B.M., Haftka, R.T., Johnson, E.R. and Farley, G.L. 1998. "Variable Complexity Design of Composite Fuselage Frames by Response Surface Techniques," Thin-Walled Structures, 32: 235-261.

17. Sun, C. T. and S. R. Kelly. 1988. "Failure in Composite Angle Structures Part II: Onset of Delamination," *Journal of Reinforced Plastics and Composites*, 7: 233-244.

18. Lekhnitskii, S. G. 1968. *Anisotropic Plates.* Gordon and Breach Publishers, pp. 95-101.

19. *ABAQUS Users Manual,* Version 6.7-1, ABAQUS, Inc. 2007.

20. ASTM D3039 – 00, "Standard Test Method for Tensile Properties of Polymer Matrix Composite Materials," American Society of Testing Materials.

21. ASTM 3518 – 94, "Standard Test Method for In-Plane Shear Response of Polymer Matrix Composite Materials by Tensile Test of a ± 45° Laminate," American Society of Testing Composite Materials.

22. Kim, R. Y. Unpublished data.

23. Tibbetts, G. G., M. L. Lake, K. L. Strong, and B. P. Rice. 2007. "A Review of the Fabrication and Properties of Vapor-Grown Carbon Nanofiber/Polymer Composites," *Composites Science and Technology*, 67: 1709-1718.

24. Lafdi, K. and K. M. Matzek. "Carbon Nanofibers as a Nano-Reinforcement for Polymeric Nanocomposites," presented at the 35th International SAMPE Technical Conference Proceedings, September-October 2003.